

Nematic correlations and nematic Berezinskii-Kosterlitz-Thouless transition in spin-1 kagome lattice antiferromagnets

Chun-Jiong Huang,^{1,2,*} Xu-Ping Yao,^{3,*} and Gang v. Chen^{4,5,†}

¹*Department of Physics and HKU-UCAS Joint Institute for Theoretical and Computational Physics at Hong Kong, The University of Hong Kong, Hong Kong, China*

²*The University of Hong Kong Shenzhen Institute of Research and Innovation, Shenzhen 518057, China*

³*Kavli Institute for Theoretical Sciences, University of Chinese Academy of Sciences, Beijing 100190, China*

⁴*International Center for Quantum Materials, School of Physics, Peking University, Beijing 100871, China*

⁵*Collaborative Innovation Center of Quantum Matter, Beijing 100871, China*

(Dated: July 24, 2025)

Nematicity plays an important role in strongly correlated electron systems. We explore the spin nematicity of a spin-1 kagome lattice antiferromagnet with the bilinear-biquadratic model and single-ion anisotropy using a generalized semiclassical approximation and Monte Carlo simulations. We reveal a rich ground state phase diagram, characterized by two main regions: a pure spin nematic phase and a region featuring the coexistence of a classical spin liquid and ferroicities for both dipolar and quadrupolar moments. The thermal fluctuation melts the spin nematic order into a critical phase with a quasi-long-range nematic order. Due to the fluctuating vortices of the spin nematic order, this critical phase further undergoes a nematic Berezinskii-Kosterlitz-Thouless transition to a paramagnetic phase, marked by an anomalous stiffness jump. Additionally, the single-ion anisotropy leads to weak ferromagnetism, resulting in spontaneous time-reversal symmetry breaking at very low temperatures. Remarkably, both two types of ferroic ordering are accompanied by classical spin liquid behaviors. Our results provide an intriguing glimpse into the interplay between geometric frustration and intertwining spin orders with different ranks, and are expected to stimulate further studies on spin-1 systems and relevant materials.

I. INTRODUCTION

Nematic liquid crystals are a well-known subject in modern soft condensed matter physics [1]. Their emergence and fluctuations in strongly correlated electronic systems have advanced our understanding of high-temperature superconductivity and fermion criticality. Electronic nematicity is often associated with the orientation of fermion bilinears and thus breaks spatial symmetry [2]. It often does not directly impact electron spins, except through spin-orbit coupling. Although spin nematicity could occur spatially, it could emerge by breaking the internal spin rotational symmetry [3–8]. In this work, we address the fluctuations and correlations of the spin nematicity of a spin-1 kagome lattice antiferromagnet.

Kagome systems [9] have been an enduring focus in quantum materials due to their versatility in realizing novel quantum phases. With such a unique geometry, the electronic structure features many nontrivial ingredients, including flat bands, Dirac band touching, and Van Hove singularities. Once the correlation effects are considered, the intertwining and competition between these ingredients trigger the emergence of a plethora of exotic phenomena, including electron band topologies [10–13], the quantum anomalous Hall effect [14, 15], the fractional quantum Hall effect [16], unconventional superconductivity and density wave orders [17–21], and so on [22].

On top of these, the geometric frustration further complicates the kagome physics and provides a promising route toward the long-sought quantum spin liquids [23–25]. Major efforts have been devoted to the spin-1/2 kagome lattice Heisenberg antiferromagnet, and a conclusion about the quantum spin liquid has not yet been reached. In contrast to the spin-1/2 moment, the spin-1 moment has a larger local Hilbert space and allows for more possibilities for new physics [26–36]. There have been several spin-1 kagome lattice antiferromagnets. Although the candidate materials $\text{Na}_2\text{Ta}_3\text{Cl}_8$ [37], $m\text{-MPYNN}\cdot\text{BF}_4$ [38–40], and $\text{KV}_3\text{Ge}_2\text{O}_9$ [41, 42] undergo a structural transition and/or lattice distortion at low temperatures and thus favor the trimerized magnetic phase due to the spin-lattice coupling [37], the newly synthesized compound $\beta\text{-BaNi}_3(\text{VO}_4)_2(\text{OH})_2$ seems to retain perfect kagome lattice geometry [43]. Experimental study of them is quite limited at this stage, and more feedback on the theoretical understanding is needed.

We consider the Heisenberg model with a biquadratic interaction and single-ion anisotropy for a spin-1 kagome lattice antiferromagnet. This model is the simplest and most generic model for spin-1 moments [7, 44–50], and the biquadratic interaction provides the direct interaction for the spin nematics. The antiferromagnetic bilinear and ferromagnetic biquadratic interactions play quite different roles in frustrated magnets. The former exhibits an extensively degenerate ground state in the classical limit. This classical degeneracy is characterized by the vanishing spin order within each triangular plaquette, accompanied by a finite configurational entropy density and a power-law decay of correlations. This

* These authors contributed equally.

† chenxray@pku.edu.cn

physics is often called classical spin liquids (CSLs) [51–53]. In contrast, the ferromagnetic biquadratic interaction simply favors a ferroquadrupolar (FQ) order. This spin nematic type of order breaks the continuous spin symmetry and is forbidden at finite temperatures by the Hohenberg-Mermin-Wagner theorem [54, 55]. Instead, a Berezinskii-Kosterlitz-Thouless (BKT) transition from the quasi-long-range ferroquadrupolar (spin nematic) order is expected just as an analogy to the well-understood classical XY model [56–58]. The low-energy description of the spin-nematic ferroquadrupolar state is an unconventional nonlinear σ model of the degenerate space of the real projective plane $\mathbb{R}P^2 \simeq S^2/\mathbb{Z}_2$ [59, 60]. In this target space, the topological charge is defined by the first homotopy group $\pi_1(\mathbb{R}P^2) = \mathbb{Z}_2$. The BKT behavior is driven by the proliferation of these \mathbb{Z}_2 half vortices with a fractional vorticity of 1/2 instead of 1 in the XY case.

In this work, we show that the CSL and BKT physics concurrently and naturally arise in the spin-1 model on a kagome lattice and reveal their intricate intertwining. At the zero temperature and for a pure FQ state with dominant K/J , the analysis of quantum fluctuations indicates an instability at $K_c/J = 2$, where a flat band of spin excitations reaches zero energy and manifests the CSL correlation in the dipole channel while the FQ correlation persists. After the phase transition, the nonzero dipolar components define three different phases at the semiclassical level in the presence of single-ion anisotropy. For all three phases, there is a nontrivial extensive degeneracy on the kagome lattice. Specifically, for both dipoles and quadruples, a ferromagnetic (ferroquadrupolar) order can be separated, leaving a degenerate part whose summation is zero within any triangular plaquette. This unusual coexistence is confirmed by our semiclassical Monte Carlo simulations. We further establish the finite-temperature phase diagram and investigate the evolution of coexisting states versus temperature. An anomalous BKT transition driven by the half vortices is numerically advocated in both pure FQ and coexistence regimes for $K/J \gtrsim 0.546$. Moreover, the CSL behavior is carefully studied at low temperatures. After a conventional crossover from the paramagnetic phase, pinch-point singularities in the dipole and quadruple spin correlations are developed and maintained to the lowest temperature in the simulation. Although there is an Ising transition due to the single-ion anisotropy at lower temperatures which is accompanied by spin-correlation enhancements at the Γ and \mathbf{K} points, a thermal order-by-disorder effect for CSLs cannot be determined.

The rest of this work is organized as follows. Section II describes the bilinear-biquadratic model for the spin-1 moments on the kagome lattice with an easy-axis single-ion anisotropy. Then, $SU(3)$ spin operators are introduced to represent the spin-1 model in a more convenient form. Based on this representation, the $SU(3)$ coherent states are defined and treated by a semiclassical approximation. With the semiclassical energy optimization, the ground-state phase diagrams are obtained

and presented in Fig. 1(a). The ground-state degeneracy and coexistence are also discussed in detail. In Sec. III, a semiclassical Monte Carlo method is introduced to simulate the finite-temperature behavior. A representative phase diagram of spin exchange interactions and temperature is shown in Fig. 1(b). The various phase transitions, especially the anomalous BKT transition and the Ising transition, are thoroughly studied. An analysis of the possible thermal order-by-order effect is also carried out numerically. Finally, we discuss the fruitful physics of this model and future research directions in Sec. IV.

II. BILINEAR-BIQUADRATIC MODEL AND SEMICLASSICAL GROUND STATES

A. Model and semiclassical approximation

The bilinear-biquadratic (BBQ) model for a spin-1 kagome lattice antiferromagnet with easy-axis single-ion anisotropy is given as

$$\mathcal{H} = \sum_{\langle ij \rangle} [J \mathbf{S}_i \cdot \mathbf{S}_j - K (\mathbf{S}_i \cdot \mathbf{S}_j)^2] - \sum_i D_z (S_i^z)^2. \quad (1)$$

Physically, the biquadratic interaction could arise from the high-order perturbation of the Hubbard model, or effectively from the spin-lattice coupling by integrating out the bond phonon modes [37, 61, 62]. It has a strong influence on the low-dimensional weak Mott insulators, particularly the two-dimensional van der Waals magnets [48]. Often, it is subordinate to the Heisenberg interaction in strength, but is important for stabilizing the spin nematicity. In addition, ultracold atomic gases or polar molecules on optical lattices provide an ideal platform to reach high internal spin degrees of freedom (DOFs) and thus allow for the exploration of a general BBQ model beyond the perturbation regime [63]. The single-ion anisotropy arises from the planar geometry of the magnets, and can also be realized and tuned with ultracold atoms [64].

We introduce the (spin bilinear) quadrupole moments $\mathbf{Q}_i = (Q_i^{x^2-y^2}, Q_i^{3z^2}, Q_i^{xy}, Q_i^{xz}, Q_i^{yz})$. For example, $Q_i^{xy} \equiv S_i^x S_i^y + S_i^y S_i^x$ (full definitions are given in the Supplemental Material (SM) [65]). With this choice, the model in Eq. (1), up to a constant, is written as

$$\mathcal{H} = \sum_{\langle ij \rangle} \left[\left(J + \frac{K}{2} \right) \mathbf{S}_i \cdot \mathbf{S}_j - \frac{K}{2} \mathbf{Q}_i \cdot \mathbf{Q}_j \right] - \sum_i D_z (S_i^z)^2. \quad (2)$$

The spin dipolar and quadrupolar DOFs are now placed on equal footing in terms of the ordering and fluctuations. Moreover, the single-ion anisotropy polarizes the Q^{3z^2} component.

With the quadrupolar interaction, the conventional large- S semiclassical treatment can no longer be applied. Since all spin states are connected

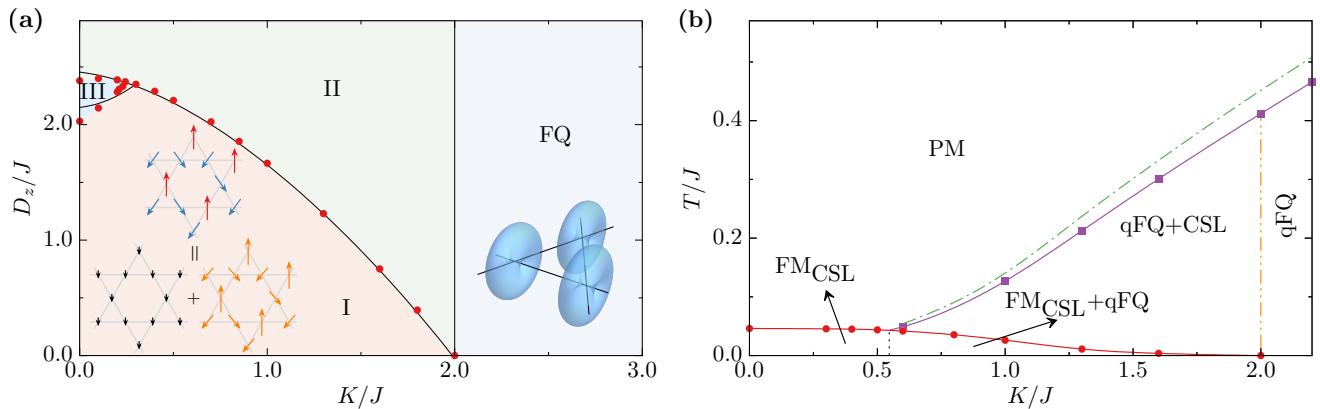


FIG. 1. (a) Ground-state phase diagram with boundaries determined by energy optimization (lines) and simulated annealing (dots) using the semiclassical Monte Carlo method. The inset in the ferroquadrupolar (FQ) phase indicates the probabilities $|\langle \mathbf{\Omega} | \mathbf{Z} \rangle|^2$ on a triangular plaquette. Explicit spin configurations for each phase and the definition of the SU(3) coherent state $|\mathbf{\Omega}\rangle$ can be found in the SM [65]. The decomposition of dipolar moments $\langle \mathbf{S}_i \rangle$ for phase I is shown in the left inset. A uniform ferromagnetic (FM) component can be singled out so that the rest sum to zero on each triangle plaquette. (b) Finite-temperature phase diagram with $D_z/J = 1.0$. There are four phases: the paramagnetic (PM) phase, the quasi-long-range FQ (qFQ) + classical spin liquid (CSL) phase, the $\text{FM}_{\text{CSL}} + \text{qFQ}$ phase and the FM_{CSL} phase for weak K/J . The purple line indicates the nematic BKT transition between the PM and qFQ+CSL or qFQ phases. At lower temperatures, an Ising transition (red line) induced by the weak FM can be determined by the Binder ratio with $L = 12, 24, 36, 48$. The system acquires CSL features from the emergence of the local restrictions (8) and (9) after a crossover (green dash-dotted line). The BKT transition disappears below $K/J \approx 0.546$, indicated by the purple line with squares, which is determined with $L = 12, 24, 36, 48, 72, 96$. The error bars of the Ising and BKT phase boundaries are smaller than the point sizes.

by the dipole and quadrupole moments, to capture this property, we instead use a semiclassical SU(3) approximation. In the spirit of “semiclassics,” we consider an entanglement-free trial wave function, $|\Psi\rangle = \prod_i |\mathbf{Z}_i\rangle$, with $|\mathbf{Z}_i\rangle = \sum_{\alpha=x,y,z} Z_i^\alpha |\alpha\rangle_i$, where $|x\rangle = \frac{1}{\sqrt{2}}(|1\rangle - |\bar{1}\rangle)$, $|y\rangle = \frac{1}{\sqrt{2}}(|1\rangle + |\bar{1}\rangle)$, and $|z\rangle = -i|0\rangle$ such that $S^\alpha |\alpha\rangle = 0$. Such a basis is intrinsically designed for a quantum state that lacks dipolar order and is instead characterized by quadrupolar order. Here, $\mathbf{Z}_i = (Z_i^x, Z_i^y, Z_i^z)^T$ is a complex vector and is constrained by the normalization condition $\mathbf{Z}_i^\dagger \cdot \mathbf{Z}_i = 1$. $|\mathbf{Z}_i\rangle$ is known as the SU(3) coherent state that forms an over-complete and non-orthogonal spin basis. All three spin states in the $S = 1$ Hilbert space are now treated on equal footing, which is called the SU(3) approximation. Thus, this semiclassical SU(3) approximation can be thought of as a *semiquantum* treatment. In this approximation, the *semiclassical* variational energy of the system is given as $H_v = \langle \Psi | \mathcal{H} | \Psi \rangle$, with

$$H_v = \sum_{\langle ij \rangle} J |\mathbf{Z}_i^\dagger \cdot \mathbf{Z}_j|^2 - (J + K) |\mathbf{Z}_i \cdot \mathbf{Z}_j|^2 + \sum_i D_z |Z_i^z|^2,$$

where the constant term has been dropped. The ground-state diagram, after H_v is optimized directly, is presented in Fig. 1(a).

B. FQ state and its instability

The most notable feature in the phase diagram of Fig. 1(a) is that the pure FQ state, where $|\langle \mathbf{Q} \rangle|$ reaches its maximum, is favored when $K/J > 2$ regardless of the single-ion anisotropy. This state is time reversal invariant and has a universal $|\mathbf{Z}_i\rangle = \cos \phi |x\rangle_i + \sin \phi |y\rangle_i$, where ϕ is interaction dependent. The real vector \mathbf{Z} is also known as the nematic director. The vanishing of the imaginary part of \mathbf{Z} indicates the absence of the dipole moment $\langle \mathbf{S} \rangle = 0$. The presence of the easy-axis anisotropy term merely requires \mathbf{Z} to lie on the x - y plane at zero temperature.

The well-ordered FQ state is exact even at the quantum limit and has no classical counterpart. Hidden in this simple ordering, the quantum fluctuation is a bit nontrivial, especially near the phase boundary $K_c/J = 2$ due to the frustrated nature of the kagome lattice. To reveal this property, we rewrite the Cartesian basis in terms of creating three different Schwinger bosons with

$$b_{i\alpha}^\dagger |\emptyset\rangle \equiv |\alpha\rangle, \quad (\alpha = x, y, z). \quad (3)$$

This representation enlarges the fundamental representation at each site, and we need to reinstate the physical Hilbert space by imposing a single-occupancy constraint,

$$\sum_{\alpha=x,y,z} b_{i\alpha}^\dagger b_{i\alpha} = 1. \quad (4)$$

The Hamiltonian in Eq. (2) can be reexpressed in terms

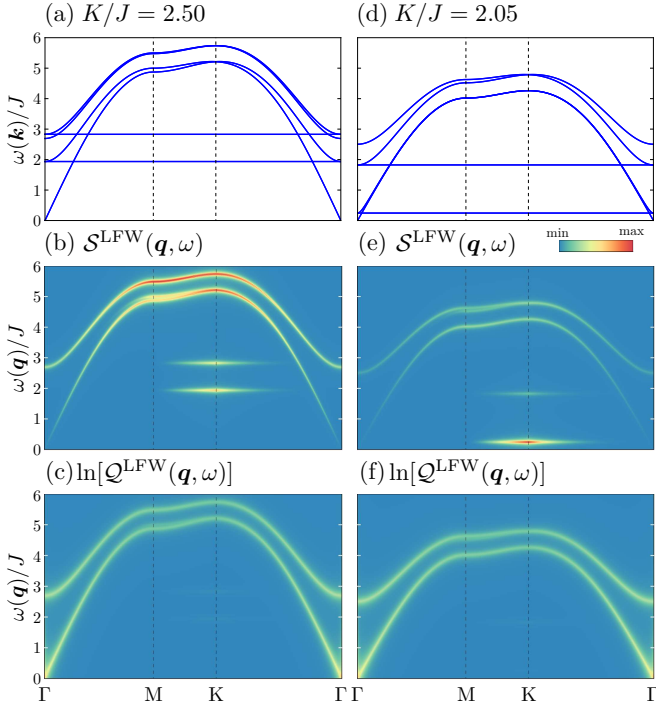


FIG. 2. The evolution of spin excitation spectra in the FQ phase. (a) The dispersions of spin excitations, (b) dipolar dynamical SFF $\mathcal{S}^{\text{LFW}}(\mathbf{q}, \omega)$, and (c) quadrupolar dynamical SFF $\mathcal{Q}^{\text{LFW}}(\mathbf{q}, \omega)$. The parameters $(K, D_z)/J = (2.5, 1.0)$ are deep in the FQ phase. (d)-(f) The equivalent results near the phase boundary with $(K, D_z)/J = (2.05, 1.0)$. The dynamical SSFs in the quadrupolar channel are displayed on a logarithmic scale for clarity.

of the Schwinger bosons,

$$\mathcal{H} = \sum_{\langle ij \rangle} J b_{i\alpha}^\dagger b_{j\alpha} b_{j\beta}^\dagger b_{i\beta} - (J + K) b_{i\alpha}^\dagger b_{j\alpha}^\dagger b_{j\beta} b_{i\beta} + D_z \sum_i b_{iz}^\dagger b_{iz}, \quad (5)$$

where the repeated Greek indices should be summarized over three flavors.

Without loss of generality, it is assumed that the flavor x of Schwinger bosons is condensed at each site in the FQ phase via the following substitution:

$$b_{i,x}^\dagger = b_{i,x} \approx 1 - \frac{1}{2}(b_{i,y}^\dagger b_{i,y} + b_{i,z}^\dagger b_{i,z}). \quad (6)$$

After the Fourier transition, the linear flavor-wave (LFW) Hamiltonian can be expressed as

$$H(\mathbf{k}) = \begin{pmatrix} \psi_{\mathbf{k}}^\dagger & \psi_{-\mathbf{k}} \end{pmatrix} \begin{pmatrix} A_{\mathbf{k}} + C & B_{\mathbf{k}} \\ B_{\mathbf{k}}^\dagger & A_{-\mathbf{k}}^* + C \end{pmatrix} \begin{pmatrix} \psi_{\mathbf{k}} \\ \psi_{-\mathbf{k}} \end{pmatrix}, \quad (7)$$

with the basis $\psi_{\mathbf{k}}^\dagger = (b_{\mathbf{k}1y}^\dagger, b_{\mathbf{k}2y}^\dagger, b_{\mathbf{k}3y}^\dagger, b_{\mathbf{k}1z}^\dagger, b_{\mathbf{k}2z}^\dagger, b_{\mathbf{k}3z}^\dagger)$. The number index labels three sublattices. The technical details and the full form of $H(\mathbf{k})$ can be found in Ref. [65]. The standard diagonalization procedure leads

to six branches of LFW excitations. In addition to the Goldstone mode characteristic of the continuous symmetry breaking of the FQ ordering, there are two flat bands in the LFW excitation spectra. Specifically, one of them has the dispersion $\omega(\mathbf{k}) = 2\sqrt{3K(K-2J)}$, which is independent of the single-ion anisotropy D_z . With the decreasing of K/J , this flat band $\omega(\mathbf{k})$ approaches zero and vanishes at $K_c/J = 2$, as shown in Figs. 2(a) and 2(d), suggesting strong instability of the FQ order. This naturally explains the D_z independence of the FQ phase boundary in Fig. 1(a).

To elucidate the impact of quantum fluctuations, we calculate the dynamical spin structure factors (SSFs) in the dipole and quadrupole channels [denoted by $\mathcal{S}^{\text{LFW}}(\mathbf{q}, \omega)$ and $\mathcal{Q}^{\text{LFW}}(\mathbf{q}, \omega)$, respectively]. The results with a logarithmic rescaling for $\mathcal{Q}^{\text{LFW}}(\mathbf{q}, \omega)$ are displayed in the second and third rows of Fig. 2. The dynamical SSFs on two flat bands are almost entirely contributed by the dipolar DOF. With the decreasing of K/J , the dynamical SSFs in the dipolar channel $\mathcal{S}^{\text{LFW}}(\mathbf{q}, \omega)$ are drastically redistributed and gradually concentrate on the lowest flat band $\omega(\mathbf{k})$, especially near the momentum \mathbf{K} , as shown in Fig. 2(e). However, such a broad peak cannot be regarded as a precursor of the conventional three-sublattice antiferromagnetic order as clarified in Ref. [65]. In contrast, three coexisting phases are obtained at the semiclassical level, as described in the next section.

C. Semiclassical ground states in the coexistence regime

After this phase transition, the dipole moments acquire nonzero expectation values $\langle \mathbf{S}_i \rangle = \langle \mathbf{Z}_i | \mathbf{S}_i | \mathbf{Z}_i \rangle$ and increase gradually with the decreasing of K/J . Three phases with distinct symmetries can be identified, and in each phase, the optimization of H_v gives three different single-site states. The only restriction on optimizing H_v is that each triangular plaquette should host all three single-site states in a given configuration. This restriction implies an extensive degeneracy on the kagome lattice. The configuration of dipole moments can be decomposed into two parts, as shown in the inset in Fig. 1(a) for phase I,

$$\sum_{i \in \Delta} \langle \mathbf{S}_i \rangle = 3\mathbf{S}_{\text{FM}} + \sum_{i \in \Delta} \langle \mathbf{S}'_i \rangle = 3\mathbf{S}_{\text{FM}}, \quad (8)$$

where the ferromagnetic (FM) component \mathbf{S}_{FM} is nonzero for $D_z > 0$ and spontaneously breaks the time-reversal symmetry. The remaining part serves as a local constraint on each triangular plaquette $\sum_{i \in \Delta} \langle \mathbf{S}'_i \rangle = 0$ with unequal length $|\langle \mathbf{S}'_i \rangle|$. Here, the dipolar and quadrupolar DOFs are intricately intertwined in the semiclassical SU(3) approximation. Corresponding to the dipole moments, three different quadruple moments $\langle \mathbf{Q}_i \rangle = \langle \mathbf{Z}_i | \mathbf{Q}_i | \mathbf{Z}_i \rangle$ are obtained. Similarly, a nonzero FQ com-

ponent can be separated,

$$\sum_{i \in \Delta} \langle \mathbf{Q}_i \rangle = 3\mathbf{Q}_{\text{FQ}} + \sum_{i \in \Delta} \langle \mathbf{Q}'_i \rangle = 3\mathbf{Q}_{\text{FQ}}, \quad (9)$$

where the remaining part analogously serves as a local constraint $\sum_{i \in \Delta} \langle \mathbf{Q}'_i \rangle = 0$ on quadrupole moments. The two local constraints for $\langle \mathbf{S}'_i \rangle$ and $\langle \mathbf{Q}'_i \rangle$ are the hallmarks of CSLs and are responsible for the extensive degeneracy of the ground states and the low-temperature spin correlations [53]. Phases II and III are identified with different spin configurations within the triangular plaquette but can be understood in the same manner [65]. We thus regard the phases in the coexistence regime as a composite of a CSL and ferroicities for both dipolar and quadrupolar DOFs.

III. FINITE TEMPERATURE PHASES AND THEIR PROPERTIES

A. Semiclassical Monte Carlo method

In parallel to the optimization of ground-state energy, the finite-temperature spin correlations for both dipolar and quadrupolar channels can be evaluated using a modified self-consistent Gaussian approximation [65]. Although certain features are not well captured by this approximation due to the loss of SU(3) commutation relations, it does qualitatively capture some of the spin correlations. To better extract the finite-temperature properties of Eq. (1), we resort to the semiclassical Monte Carlo (sMC) algorithm [47]. This method is based on the variational energy H_v that is extended to finite temperatures. The sampling in the simulation, with a standard Metropolis algorithm as the primary method, is made up of the entanglement-free direct product of quantum states defined previously by $|\Psi\rangle$. The partition function $\mathcal{Z} = \text{Tr}[\exp(-\beta\mathcal{H})]$ can be approximated as

$$\mathcal{Z} \approx \int \prod_i d\mathbf{Z}_i e^{-\beta\langle\Psi|\mathcal{H}|\Psi\rangle} = \int \prod_i d\mathbf{Z}_i e^{-\beta H_v}, \quad (10)$$

where H_v is a real number. Now the partition function is an integration over a set of complex vectors \mathbf{Z}_i 's without the infamous sign problem. In every Metropolis update, a random site i is selected, and a new vector \mathbf{Z}'_i is proposed near the current vector \mathbf{Z}_i randomly. The energy difference $\Delta E = E_{\text{new}} - E_{\text{current}}$ is calculated between the energies of the new configuration, E_{new} , and of the current configuration, E_{current} . If $\Delta E < 0$, the vector on site i is updated to \mathbf{Z}'_i . Otherwise, this update is accepted with a probability $e^{-\beta\Delta E}$. In addition, the overall phase of each site is considered to make the random sampling \mathbf{Z}'_i more efficient. This step will not change the physics because all the observables we are interested in are gauge invariant.

Meanwhile, a microcanonical relaxation technique proposed in Ref. [66] is employed to reduce autocorrelation,

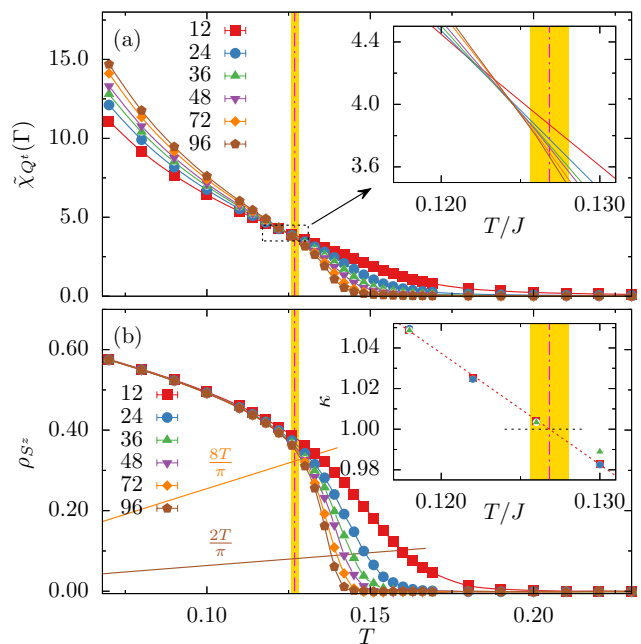


FIG. 3. Scaled susceptibility $\tilde{\chi}_{Q^t}$ and stiffness ρ_{S^z} for $(K, D_z)/J = (1.0, 1.0)$. At the nematic BKT transition temperature $T_{\text{BKT}} = 0.127(1)$ (pink dash-dotted line, with the yellow region acting as an error bar), (a) $\tilde{\chi}_{Q^t}$ has an intersection, and (b) ρ_{S^z} has a jump. The orange and brown solid lines refer to functions $f(T) = 8T/\pi$ and $g(T) = 2T/\pi$, respectively. The inset in (b) shows solutions of RG equations and their linear fit for different pairs of system sizes.

which is similar to the over-relaxation technique used in the classical continuous spin model [67, 68]. Specifically, a local unitary transformation $e^{ic\mathcal{H}_i^l} |\mathbf{Z}_i\rangle$ is introduced. The energy of the system within the semiclassical SU(3) approximation is preserved under this transformation. The local operator \mathcal{H}_i^l on site i is defined by $\mathcal{H}_i^l = (\otimes_{j \neq i} \langle \mathbf{Z}_j |) \mathcal{H} (\otimes_{j \neq i} |\mathbf{Z}_j\rangle)$, or, more explicitly,

$$\mathcal{H}_i^l = \sum_{\langle ij \rangle} \left[\left(J + \frac{K}{2} \right) \mathbf{S}_i \cdot \langle \mathbf{S} \rangle_j - \frac{K}{2} \mathbf{Q}_i \cdot \langle \mathbf{Q} \rangle_j \right] - \sum_i D_z (S_i^z)^2. \quad (11)$$

The real number c is chosen uniformly in the region $[-\pi\alpha^{-1}, \pi\alpha^{-1}]$, with α being the Frobenius norm of the matrix form of \mathcal{H}_i^l .

Additionally, parallel tempering is implemented near the Ising transition to overcome the non-ergodic problem [69]. It offers a solution by running multiple replicas of the system at different temperatures simultaneously and exchanging configurations between them. The low-temperature replicas can more efficiently explore the configuration space by exchanging configurations with a high-temperature replica whose autocorrelation time is short. This leads to sampling improvements to statistically independent configurations and enables meaningful statistical analysis. In our simulations, the probability of exchanging replicas is in the range of about 0.3 to 0.5.

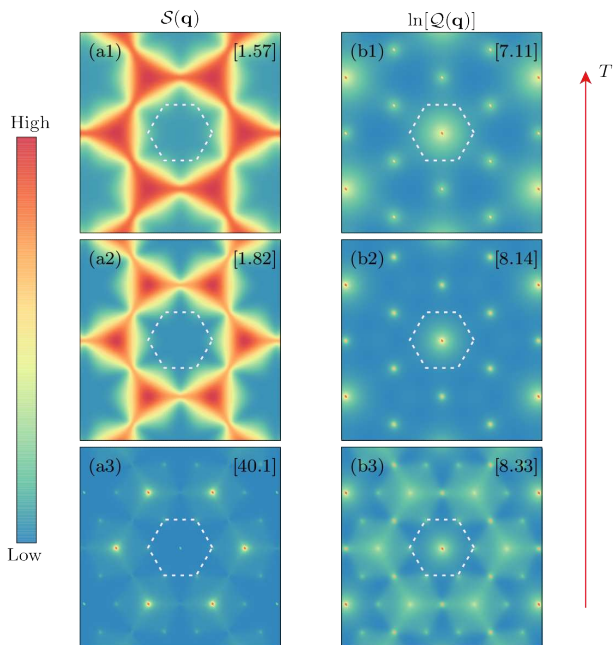


FIG. 4. Dipolar and quadrupolar SSFs, $S(\mathbf{q})$ and $Q(\mathbf{q})$, at $(K, D_z)/J = (1.0, 1.0)$ with $L = 48$. The intensities are normalized with the maximum (number in the top right) in every graph. From top to bottom, the temperature decreases from $T/J = 0.2$ to 0.079 to 0.016 . The system is sequentially in the PM, qFQ+CSL, and FM_{CSL}+qFQ phases. The dashed hexagon is the first Brillouin zone. The region in the momentum space corresponds to $-4\pi \leq q_{x,y} \leq 4\pi$.

B. Finite phases and phase transitions

The generic finite-temperature phase diagram from the sMC simulations is depicted in Fig. 1(b) with the represented value $D_z = J$. We utilize the specific heat, the fluctuation of dipolar or quadrupolar moment, the quadrupolar susceptibility $\chi_{Q^t}(\mathbf{q}) = \beta \langle |Q^t(\mathbf{q})|^2 \rangle / N$ [where $Q^t = (Q^{x^2-y^2}, Q^{xy})$ and N is the number of spins] and the spin stiffness $\rho_{S^z} = \{ \langle \partial^2 F(\theta) / \partial \theta^2 \rangle - \beta \langle (\partial F(\theta) / \partial \theta)^2 \rangle \} / N|_{\theta=0}$ [where $F(\theta)$ is the twisted free energy] to determine phase boundaries (see the detailed definition in the SM [65]). We have simulated for other finite D_z 's, and the basic structure of the phase diagram remained unchanged.

In Fig. 1(b), only one direct transition (purple line with squares) occurs for $K > 2J$, where the system exhibits a quasi-long-range FQ (qFQ) order below the transition and a true long-range spin nematic order at $T = 0$. This transition is further identified as a nematic BKT transition. Given the failure of specific heat to determine this topological transition [70], the scaled susceptibility $\tilde{\chi}_{Q^t} = L^{2-\eta} (\ln L)^{1/8} \chi_{Q^t}$ (where L is the system size) and the stiffness ρ_{S^z} are employed [71]. For $\tilde{\chi}_{Q^t}$ in Fig. 3(a), the critical exponent η is set to $1/4$ and belongs to the BKT universality class. At the transition, there is an intersection with different system sizes. The criti-

cal value of the stiffness at the transition temperature T_c is $(\rho_{S^z})_c = 8T_c/\pi$, 4 times larger than the conventional value as a consequence of the \mathbb{Z}_2 half vortices with the fractional vorticity of $1/2$ instead of 1 in the standard XY universality class [66, 72]. This fractional vorticity, rooted in the $\mathbb{R}P^2$ space of \mathbf{Q} , has a topological origin distinct from those in generalized XY models [73–76]. The data were further subjected to finite-size scaling using the BKT renormalization group equation $4 \ln(L_2/L_1) = \int_{R_2}^{R_1} dt / [t^2 (\ln t - \kappa) + t]$, where $R = \pi \rho_{S^z} / 8T$ and $L_1 < L_2$ are two different system sizes. The size-independent parameter κ follows $\kappa(T) = 1 + \kappa'(T_c - T)$ near T_c [77]. The well-fitted $\kappa(T)$ curve and the critical point $\kappa(T_c) = 1$ are shown in the inset of Fig. 3(b). All analyses unanimously advocate the BKT transition, with the critical point indicated by pink dash-dotted lines in Fig. 3.

Slightly above T_c , a conventional crossover can be simultaneously identified in the specific heat and the susceptibility of local constraints [65]. It is thus attributed to the emergence of CSLs [green dash-dotted line in Fig. 1(b)]. For $0.546J \lesssim K < 2J$, while the nematic BKT transition persists, an additional transition occurs at a lower temperature with a weak ferromagnetic order [red line in Fig. 1(b)]. This order is rooted in the residual FM part of Eq. (8). Due to the time-reversal symmetry breaking, this lower-temperature transition is of the Ising type (see the SM [65] for more evidence). For $K \lesssim 0.546J$, the nematic BKT transition can not be maintained given the strong dipolar frustration, and only the Ising transition and the CSL crossover survive, although the crossover is indistinguishable in terms of χ_λ (see Fig. S8 in the SM [65]).

To further characterize different finite-temperature phases, we compute the SSFs $\mathcal{A}(\mathbf{q}) = \sum_{m,n} \langle \mathbf{A}^m(\mathbf{q}) \cdot \mathbf{A}^n(-\mathbf{q}) \rangle / N$ (m and n are sublattice indexes) for both dipolar ($\mathcal{A} = \mathcal{S}$) and quadrupolar ($\mathcal{A} = \mathcal{Q}$) moments. The results for $(K, D_z)/J = (1.0, 1.0)$ and $L = 48$ are depicted in Fig. 4 at three different temperatures. For clarity, the intensities of $Q(\mathbf{q})$ are taken in the logarithmic scale. In the featureless paramagnetic (PM) phase, broad peaks appear for both $S(\mathbf{q})$ and $Q(\mathbf{q})$ [Figs. 4(a₁) and (b₁)]. After a conventional crossover whose temperature is slightly higher than that of the nematic BKT type, pinch points gradually take shape at $2\mathbf{M}$ and symmetry-equivalent points in the dipolar channel, as shown in Fig. 4(a₂). This pattern in the SSF reveals the development of CSLs. In the quadrupolar channel, the intensity of $Q(\mathbf{q})$ in Fig. 4(b₂) is further concentrated near the Γ point after the nematic BKT transition due to the formation of qFQ order. Further cooling would drive the system into a new phase via an Ising transition. Intensifications of $S(\mathbf{q})$ and $Q(\mathbf{q})$ occur at the $2\mathbf{K}$ and \mathbf{K} points, while the pinch points become visible in both channels because of the enhanced effect of local constraints at the low-temperature limit. Within the system size we simulated, the intensity $S(\mathbf{K})$ decreases with L (see Fig. S10 in the SM [65]). Moreover, the

specific heat remains no less than 2 (four DOFs for \mathbf{Z}_i) down to the lowest temperature, suggesting the absence of soft modes in the excitation spectrum [see Fig. S6(a) in the SM [65]]. Therefore, the thermal order-by-disorder effect, if it exists, is speculated to notably differ from the fully classical model with O(3) vector spins in which coplanar states are selected [78, 79]. In addition, the residual FM part in Eq. (8) leads to a strong peak in $\mathcal{S}(\mathbf{q})$ at the Γ point. Therefore, we denote this low-temperature phase as FM_{CSL}+qFQ in Fig. 1(b).

IV. DISCUSSION

Within the limit of our methods, we have obtained a rich phase diagram both at zero temperature and in the finite-temperature regime. The distinct patterns of spin correlations and spin orders were carefully analyzed. The spin nematic type of quadrupolar order, which is sometimes placed into categories of hidden orders [80], generates coherent spin excitations that are very different from conventional spin-wave excitation for conventional magnetic orders. Moreover, slightly akin to charge-4e superconductors [81] (but differing in the nature of the vorticity), the melting of the spin nematic order was found to go through a nematic type of BKT transition. In the $D_z = 0$ limit on the horizontal axis in Fig. 1(a), the symmetry of the BBQ model is restored to SU(2). The energy gain from the FM component \mathbf{S}_{FM} vanishes in the ground states. The coexistence of the approximate-long-range FQ (aFQ) order and the CSL behaviors is expected. Moreover, the higher symmetry rules out the

probability of BKT transitions from the nematic ordering. As a consequence, both the Ising and BKT transitions for the $D_z = 0$ case were found to become conventional crossovers [65].

The physics of the spin-1 kagome lattice antiferromagnet contains at least three major ingredients, and they are strong geometric frustration, multipolar moments, and strong quantum fluctuations. In this work, we have mainly considered the interplay between the strong geometric frustration and the multipolar nature of the local moments. Owing to the choice of the method and the approximation, the strong quantum fluctuations were not analyzed in depth. When all three ingredients are taken into account, more exotic results may occur [3, 8]. It is well-known that, the local constraint in the classical spin liquid may turn into a matter-gauge coupled theory in the quantum regime. For the case of two constraints in dipolar and quadrupolar channels in the current problem, the resulting matter-gauge couplings in the quantum regime can have more structures and require further efforts.

ACKNOWLEDGMENTS

This work is supported by the MOST of China under Grants No. 2021YFA1400300 and No. 2022YFA1403902, by the NSFC under Grants No. 92065203 and No. 11920101005, and by the Fundamental Research Funds for the Central Universities, Peking University. C.-J. H. thanks Y. Deng for valuable discussions and for his hospitality at the University of Science and Technology of China and Z. Wang for his hospitality at Zhejiang University, where part of this work was completed.

-
- [1] D. Andrienko, Introduction to liquid crystals, *Journal of Molecular Liquids* **267**, 520 (2018).
- [2] E. Fradkin, S. A. Kivelson, M. J. Lawler, J. P. Eisenstein, and A. P. Mackenzie, Nematic Fermi Fluids in Condensed Matter Physics, *Annual Review of Condensed Matter Physics* **1**, 153–178 (2010).
- [3] M. E. Zhitomirsky and H. Tsunetsugu, Magnon pairing in quantum spin nematic, *EPL (Europhysics Letters)* **92**, 37001 (2010).
- [4] G. Chen, R. Pereira, and L. Balents, Exotic phases induced by strong spin-orbit coupling in ordered double perovskites, *Phys. Rev. B* **82**, 174440 (2010).
- [5] G. Chen and L. Balents, Spin-orbit coupling in d^2 ordered double perovskites, *Phys. Rev. B* **84**, 094420 (2011).
- [6] A. Smerald and N. Shannon, Theory of spin excitations in a quantum spin-nematic state, *Phys. Rev. B* **88**, 184430 (2013).
- [7] R. Pohle, N. Shannon, and Y. Motome, Spin nematics meet spin liquids: Exotic quantum phases in the spin-1 bilinear-biquadratic model with Kitaev interactions, *Phys. Rev. B* **107**, L140403 (2023).
- [8] S. Jiang, J. Romhányi, S. R. White, M. E. Zhitomirsky, and A. L. Chernyshev, Where is the Quantum Spin Nematic?, *Phys. Rev. Lett.* **130**, 116701 (2023).
- [9] I. Syôzi, Statistics of Kagomé Lattice, *Progress of Theoretical Physics* **6**, 306 (1951).
- [10] D. F. Liu, A. J. Liang, E. K. Liu, Q. N. Xu, Y. W. Li, C. Chen, D. Pei, W. J. Shi, S. K. Mo, P. Dudin, T. Kim, C. Cacho, G. Li, Y. Sun, L. X. Yang, Z. K. Liu, S. S. P. Parkin, C. Felser, and Y. L. Chen, Magnetic Weyl semimetal phase in a Kagomé crystal, *Science* **365**, 1282 (2019).
- [11] N. Morali, R. Batabyal, P. K. Nag, E. Liu, Q. Xu, Y. Sun, B. Yan, C. Felser, N. Avraham, and H. Beidenkopf, Fermi-arc diversity on surface terminations of the magnetic Weyl semimetal $\text{Co}_3\text{Sn}_2\text{S}_2$, *Science* **365**, 1286 (2019).
- [12] L. Ye, M. Kang, J. Liu, F. von Cube, C. R. Wicker, T. Suzuki, C. Jozwiak, A. Bostwick, E. Rotenberg, D. C. Bell, L. Fu, R. Comin, and J. G. Checkelsky, Massive Dirac fermions in a ferromagnetic kagome metal, *Nature* **555**, 638 (2018).
- [13] J.-X. Yin, W. Ma, T. A. Cochran, X. Xu, S. S. Zhang, H.-J. Tien, N. Shumiya, G. Cheng, K. Jiang, B. Lian, Z. Song, G. Chang, I. Belopolski, D. Multer, M. Litskevich, Z.-J. Cheng, X. P. Yang, B. Swidler, H. Zhou,

- H. Lin, T. Neupert, Z. Wang, N. Yao, T.-R. Chang, S. Jia, and M. Zahid Hasan, Quantum-limit Chern topological magnetism in TbMn_6Sn_6 , *Nature* **583**, 533 (2020).
- [14] G. Xu, B. Lian, and S.-C. Zhang, Intrinsic Quantum Anomalous Hall Effect in the Kagome Lattice $\text{Cs}_2\text{LiMn}_3\text{F}_{12}$, *Phys. Rev. Lett.* **115**, 186802 (2015).
- [15] E. Liu, Y. Sun, N. Kumar, L. Muechler, A. Sun, L. Jiao, S.-Y. Yang, D. Liu, A. Liang, Q. Xu, J. Kroder, V. Süß, H. Borrmann, C. Shekhar, Z. Wang, C. Xi, W. Wang, W. Schnelle, S. Wirth, Y. Chen, S. T. B. Goennenwein, and C. Felser, Giant anomalous Hall effect in a ferromagnetic kagome-lattice semimetal, *Nature Physics* **14**, 1125 (2018).
- [16] E. Tang, J.-W. Mei, and X.-G. Wen, High-Temperature Fractional Quantum Hall States, *Phys. Rev. Lett.* **106**, 236802 (2011).
- [17] W.-H. Ko, P. A. Lee, and X.-G. Wen, Doped kagome system as exotic superconductor, *Phys. Rev. B* **79**, 214502 (2009).
- [18] B. R. Ortiz, S. M. L. Teicher, Y. Hu, J. L. Zuo, P. M. Sarte, E. C. Schueller, A. M. M. Abeykoon, M. J. Krogstad, S. Rosenkranz, R. Osborn, R. Seshadri, L. Balents, J. He, and S. D. Wilson, CsV_3Sb_5 : A \mathbb{Z}_2 Topological Kagome Metal with a Superconducting Ground State, *Phys. Rev. Lett.* **125**, 247002 (2020).
- [19] Y.-X. Jiang, J.-X. Yin, M. M. Denner, N. Shumiya, B. R. Ortiz, G. Xu, Z. Guguchia, J. He, M. S. Hossain, X. Liu, J. Ruff, L. Kautzsch, S. S. Zhang, G. Chang, I. Belopolski, Q. Zhang, T. A. Cochran, D. Multer, M. Litskevich, Z.-J. Cheng, X. P. Yang, Z. Wang, R. Thomale, T. Neupert, S. D. Wilson, and M. Z. Hasan, Unconventional chiral charge order in kagome superconductor KV_3Sb_5 , *Nature Materials* **20**, 1353 (2021).
- [20] H. Li, T. T. Zhang, T. Yilmaz, Y. Y. Pai, C. E. Marvinney, A. Said, Q. W. Yin, C. S. Gong, Z. J. Tu, E. Vescovo, C. S. Nelson, R. G. Moore, S. Murakami, H. C. Lei, H. N. Lee, B. J. Lawrie, and H. Miao, Observation of Unconventional Charge Density Wave without Acoustic Phonon Anomaly in Kagome Superconductors AV_3Sb_5 ($A = \text{Rb}, \text{Cs}$), *Phys. Rev. X* **11**, 031050 (2021).
- [21] H. Chen, H. Yang, B. Hu, Z. Zhao, J. Yuan, Y. Xing, G. Qian, Z. Huang, G. Li, Y. Ye, S. Ma, S. Ni, H. Zhang, Q. Yin, C. Gong, Z. Tu, H. Lei, H. Tan, S. Zhou, C. Shen, X. Dong, B. Yan, Z. Wang, and H.-J. Gao, Roton pair density wave in a strong-coupling kagome superconductor, *Nature* **599**, 222 (2021).
- [22] J.-X. Yin, B. Lian, and M. Z. Hasan, Topological kagome magnets and superconductors, *Nature* **612**, 647 (2022).
- [23] S. Sachdev, Kagome- and triangular-lattice Heisenberg antiferromagnets: Ordering from quantum fluctuations and quantum-disordered ground states with unconfined bosonic spinons, *Phys. Rev. B* **45**, 12377 (1992).
- [24] L. Balents, Spin liquids in frustrated magnets, *Nature* **464**, 199 (2010).
- [25] C. Broholm, R. J. Cava, S. A. Kivelson, D. G. Nocera, M. R. Norman, and T. Senthil, Quantum spin liquids, *Science* **367**, eaay0668 (2020).
- [26] I. Affleck, T. Kennedy, E. H. Lieb, and H. Tasaki, Rigorous results on valence-bond ground states in antiferromagnets, *Phys. Rev. Lett.* **59**, 799 (1987).
- [27] G. Chen, M. Hermele, and L. Radzihovsky, Frustrated Quantum Critical Theory of Putative Spin-Liquid Phenomenology in $6H-\text{B}-\text{Ba}_3\text{NiSb}_2\text{O}_9$, *Phys. Rev. Lett.* **109**, 016402 (2012).
- [28] J. Q. Liu, F.-Y. Li, G. Chen, and Z. Wang, Featureless quantum paramagnet with frustrated criticality and competing spiral magnetism on spin-1 honeycomb lattice magnet, *Phys. Rev. Res.* **2**, 033260 (2020).
- [29] F.-Y. Li and G. Chen, Competing phases and topological excitations of spin-1 pyrochlore antiferromagnets, *Phys. Rev. B* **98**, 045109 (2018).
- [30] G. Chen, Quantum paramagnet and frustrated quantum criticality in a spin-one diamond lattice antiferromagnet, *Phys. Rev. B* **96**, 020412 (2017).
- [31] F.-Y. Li and G. Chen, Spin-orbital entanglement in d^8 Mott insulators: Possible excitonic magnetism in diamond lattice antiferromagnets, *Phys. Rev. B* **100**, 045103 (2019).
- [32] F. L. Buessen, M. Hering, J. Reuther, and S. Trebst, Quantum Spin Liquids in Frustrated Spin-1 Diamond Antiferromagnets, *Phys. Rev. Lett.* **120**, 057201 (2018).
- [33] S. Das, D. Nafday, T. Saha-Dasgupta, and A. Paramekanti, NiRh_2O_4 : A spin-orbit entangled diamond-lattice paramagnet, *Phys. Rev. B* **100**, 140408 (2019).
- [34] X.-Y. Dong and D. N. Sheng, Spin-1 Kitaev-Heisenberg model on a honeycomb lattice, *Phys. Rev. B* **102**, 121102 (2020).
- [35] C. Yu-Hsueh, J. Genzor, Y. B. Kim, and Y.-J. Kao, Excitation spectrum of spin-1 Kitaev spin liquids, *Phys. Rev. B* **105**, L060403 (2022).
- [36] U. F. P. Seifert and L. Savary, Phase diagrams and excitations of anisotropic $S = 1$ quantum magnets on the triangular lattice, *Phys. Rev. B* **106**, 195147 (2022).
- [37] A. Paul, C.-M. Chung, T. Birol, and H. J. Changlani, Spin-lattice Coupling and the Emergence of the Trimerized Phase in the $S = 1$ Kagome Antiferromagnet $\text{Na}_2\text{Ti}_3\text{Cl}_8$, *Phys. Rev. Lett.* **124**, 167203 (2020).
- [38] N. Wada, T. Kobayashi, H. Yano, T. Okuno, A. Yamaguchi, and K. Awaga, Observation of Spin-Gap State in Two-Dimensional Spin-1 Kagomé Antiferromagnet m-PYNN-BF_4 , *Journal of the Physical Society of Japan* **66**, 961 (1997).
- [39] T. Kambe, Y. Nogami, K. Oshima, W. Fujita, and K. Awaga, Structural Phase Transition in Two-Dimensional kagomé Antiferromagnet $\text{m-N-Methylpyridinium } \alpha\text{-nitronyl nitroxide-BF}_4 \cdot \frac{1}{3}$ (Acetone), *Journal of the Physical Society of Japan* **73**, 796 (2004).
- [40] T. Matsushita, N. Hamaguchi, K. Shimizu, N. Wada, W. Fujita, K. Awaga, A. Yamaguchi, and H. Ishimoto, Quantum Spin State and Magnetization Plateaus in an $S=1$ Kagomé Heisenberg Antiferromagnet, *Journal of the Physical Society of Japan* **79**, 093701 (2010).
- [41] S. Hara, H. Sato, and Y. Narumi, Exotic Magnetism of Novel $S = 1$ Kagome Lattice Antiferromagnet $\text{KV}_3\text{Ge}_2\text{O}_9$, *Journal of the Physical Society of Japan* **81**, 073707 (2012).
- [42] E. Takagi, T. Aoyama, S. Hara, H. Sato, T. Kimura, and Y. Wakabayashi, Structural deformation of the $S = 1$ kagome-lattice compound $\text{KV}_3\text{Ge}_2\text{O}_9$, *Phys. Rev. B* **95**, 104416 (2017).
- [43] B. Li, Z. Wan, Y. Song, Z. Ma, Y. Zhao, J. Wang, and Y. Li, Frustrated magnetism of the spin-1 kagome antiferromagnet $\beta\text{-BaNi}_3(\text{VO}_4)_2(\text{OH})_2$, *Journal of Physics: Condensed Matter* **35**, 505801 (2023).
- [44] S. Nakatsuji, Y. Nambu, H. Tonomura, O. Sakai, S. Jonas, C. Broholm, H. Tsunetsugu, Y. Qiu, and Y. Maeno, Spin Disorder on a Triangular Lattice, *Sci-*

- ence **309**, 1697 (2005).
- [45] H. Tsunetsugu and M. Arikawa, Spin Nematic Phase in $S=1$ Triangular Antiferromagnets, *Journal of the Physical Society of Japan* **75**, 083701 (2006).
- [46] A. Läuchli, F. Mila, and K. Penc, Quadrupolar Phases of the $S = 1$ Bilinear-Biquadratic Heisenberg Model on the Triangular Lattice, *Phys. Rev. Lett.* **97**, 087205 (2006).
- [47] E. M. Stoudenmire, S. Trebst, and L. Balents, Quadrupolar correlations and spin freezing in $S = 1$ triangular lattice antiferromagnets, *Phys. Rev. B* **79**, 214436 (2009).
- [48] A. Kartsev, M. Augustin, R. F. L. Evans, K. S. Novoselov, and E. J. G. Santos, Biquadratic exchange interactions in two-dimensional magnets, *npj Computational Materials* **6**, 150 (2020).
- [49] R. Pohle, N. Shannon, and Y. Motome, Eight-color chiral spin liquid in the $S = 1$ bilinear-biquadratic model with Kitaev interactions, *Phys. Rev. Res.* **6**, 033077 (2024).
- [50] R. Pohle and N. Shannon, Abundance of spin liquids in the $S = 1$ bilinear-biquadratic model on the pyrochlore lattice, and its application to $\text{NaCaNi}_2\text{F}_7$ (2025), [arXiv:2503.12776 \[cond-mat.str-el\]](https://arxiv.org/abs/2503.12776).
- [51] R. Moessner and J. T. Chalker, Properties of a Classical Spin Liquid: The Heisenberg Pyrochlore Antiferromagnet, *Phys. Rev. Lett.* **80**, 2929 (1998).
- [52] R. Moessner and J. T. Chalker, Low-temperature properties of classical geometrically frustrated antiferromagnets, *Phys. Rev. B* **58**, 12049 (1998).
- [53] C. L. Henley, The “Coulomb Phase” in Frustrated Systems, *Annual Review of Condensed Matter Physics* **1**, 179 (2010).
- [54] N. D. Mermin and H. Wagner, Absence of Ferromagnetism or Antiferromagnetism in One- or Two-Dimensional Isotropic Heisenberg Models, *Phys. Rev. Lett.* **17**, 1133 (1966).
- [55] P. C. Hohenberg, Existence of Long-Range Order in One and Two Dimensions, *Phys. Rev.* **158**, 383 (1967).
- [56] J. M. Kosterlitz and D. J. Thouless, Ordering, metastability and phase transitions in two-dimensional systems, *J. Phys. C* **6**, 1181 (1973).
- [57] J. M. Kosterlitz, The critical properties of the two-dimensional xy model, *J. Phys. C* **7**, 1046 (1974).
- [58] D. J. Amit, Y. Y. Goldschmidt, and S. Grinstein, Renormalisation group analysis of the phase transition in the 2D Coulomb gas, Sine-Gordon theory and XY-model, *J. Phys. A* **13**, 585 (1980).
- [59] B. A. Ivanov and A. K. Kolezhuk, Effective field theory for the $S = 1$ quantum nematic, *Phys. Rev. B* **68**, 052401 (2003).
- [60] B. A. Ivanov, R. S. Khymyn, and A. K. Kolezhuk, Pairing of Solitons in Two-Dimensional $S = 1$ Magnets, *Phys. Rev. Lett.* **100**, 047203 (2008).
- [61] K. Tanaka, Y. Yokoyama, and C. Hotta, Origin of Biquadratic Exchange Interactions in a Mott Insulator as a Driving Force of Spin Nematic Order, *Journal of the Physical Society of Japan* **87**, 023702 (2018).
- [62] M. Hoffmann and S. Blügel, Systematic derivation of realistic spin models for beyond-Heisenberg solids, *Phys. Rev. B* **101**, 024418 (2020).
- [63] S. R. Manmana, E. M. Stoudenmire, K. R. A. Hazzard, A. M. Rey, and A. V. Gorshkov, Topological phases in ultracold polar-molecule quantum magnets, *Phys. Rev. B* **87**, 081106 (2013).
- [64] W. C. Chung, J. de Hond, J. Xiang, E. Cruz-Colón, and W. Ketterle, Tunable Single-Ion Anisotropy in Spin-1 Models Realized with Ultracold Atoms, *Phys. Rev. Lett.* **126**, 163203 (2021).
- [65] See Supplemental Material for detailed information the $SU(3)$ approximation, optimized ground states, derivations linear flavor-wave theory and self-consistent Gaussian approximation, and definitions of observables and extensive numerical results in semiclassical Monte Carlo simulations, which includes Refs. [70, 78, 79, 82–86].
- [66] D. Yamamoto, C. Suzuki, G. Marmorini, S. Okazaki, and N. Furukawa, Quantum and Thermal Phase Transitions of the Triangular $SU(3)$ Heisenberg Model under Magnetic Fields, *Phys. Rev. Lett.* **125**, 057204 (2020).
- [67] F. R. Brown and T. J. Woch, Overrelaxed heat-bath and Metropolis algorithms for accelerating pure gauge Monte Carlo calculations, *Phys. Rev. Lett.* **58**, 2394 (1987).
- [68] M. Creutz, Overrelaxation and Monte Carlo simulation, *Phys. Rev. D* **36**, 515 (1987).
- [69] K. Hukushima and K. Nemoto, Exchange Monte Carlo Method and Application to Spin Glass Simulations, *JPSJ* **65**, 1604 (1996).
- [70] P. H. Nguyen and M. Boninsegni, Superfluid Transition and Specific Heat of the 2D x-y Model: Monte Carlo Simulation, *Applied Sciences* **11**, 4931 (2021).
- [71] B.-Z. Wang, P. Hou, C.-J. Huang, and Y. Deng, Percolation of the two-dimensional XY model in the flow representation, *Phys. Rev. E* **103**, 062131 (2021).
- [72] S. Mukerjee, C. Xu, and J. E. Moore, Topological Defects and the Superfluid Transition of the $S = 1$ Spinor Condensate in Two Dimensions, *Phys. Rev. Lett.* **97**, 120406 (2006).
- [73] D. H. Lee and G. Grinstein, Strings in two-dimensional classical XY models, *Phys. Rev. Lett.* **55**, 541 (1985).
- [74] D. B. Carpenter and J. T. Chalker, The phase diagram of a generalised XY model, *Journal of Physics: Condensed Matter* **1**, 4907 (1989).
- [75] D. M. Hübscher and S. Wessel, Stiffness jump in the generalized XY model on the square lattice, *Phys. Rev. E* **87**, 062112 (2013).
- [76] V. Drouin-Touchette, P. P. Orth, P. Coleman, P. Chandra, and T. C. Lubensky, Emergent Potts Order in a Coupled Hexatic-Nematic XY model, *Phys. Rev. X* **12**, 011043 (2022).
- [77] M. Boninsegni and N. Prokof'ev, Supersolid Phase of Hard-Core Bosons on a Triangular Lattice, *Phys. Rev. Lett.* **95**, 237204 (2005).
- [78] M. E. Zhitomirsky, Octupolar ordering of classical kagome antiferromagnets in two and three dimensions, *Phys. Rev. B* **78**, 094423 (2008).
- [79] G.-W. Chern and R. Moessner, Dipolar Order by Disorder in the Classical Heisenberg Antiferromagnet on the Kagome Lattice, *Phys. Rev. Lett.* **110**, 077201 (2013).
- [80] J. A. Mydosh and P. M. Oppeneer, Colloquium: Hidden order, superconductivity, and magnetism: The unsolved case of URu_2Si_2 , *Rev. Mod. Phys.* **83**, 1301 (2011).
- [81] E. Berg, E. Fradkin, and S. A. Kivelson, Charge-4e superconductivity from pair-density-wave order in certain high-temperature superconductors, *Nature Physics* **5**, 830 (2009).
- [82] S. G. Johnson, The NLOpt nonlinear-optimization package, <https://github.com/stevengj/nlopt> (2007).
- [83] A. S. Wills, R. Ballou, and C. Lacroix, Model of localized highly frustrated ferromagnetism: The kagomé spin ice, *Phys. Rev. B* **66**, 144407 (2002).
- [84] R. Moessner and S. L. Sondhi, Theory of the [111] mag-

- netization plateau in spin ice, *Phys. Rev. B* **68**, 064411 (2003).
- [85] J. Carrasquilla, Z. Hao, and R. G. Melko, A two-dimensional spin liquid in quantum kagome ice, *Nature Communications* **6**, 7421 (2015).
- [86] J. T. Chalker, P. C. W. Holdsworth, and E. F. Shender, Hidden order in a frustrated system: Properties of the Heisenberg Kagomé antiferromagnet, *Phys. Rev. Lett.* **68**, 855 (1992).

Supplemental Material for “Nematic correlations and nematic Berezinskii-Kosterlitz-Thouless transition in spin-1 kagomé lattice antiferromagnets”

Chun-Jiong Huang,^{1,2,*} Xu-Ping Yao,^{3,*} and Gang v. Chen^{4,5,†}

¹*Department of Physics and HKU-UCAS Joint Institute for Theoretical and Computational Physics at Hong Kong, The University of Hong Kong, Hong Kong, China*

²*The University of Hong Kong Shenzhen Institute of Research and Innovation, Shenzhen 518057, China*

³*Kavli Institute for Theoretical Sciences, University of Chinese Academy of Sciences, Beijing 100190, China*

⁴*International Center for Quantum Materials, School of Physics, Peking University, Beijing 100871, China*

⁵*Collaborative Innovation Center of Quantum Matter, Beijing 100871, China*

(Dated: July 24, 2025)

I. OPTIMIZED GROUND STATES

The presence of the biquadratic interaction in the Hamiltonian \mathcal{H} requires the finite-dimensional irreducible representation of the spin-1 moments. Therefore, it is more convenient to formulate the problem with the $\mathfrak{su}(3)$ Lie algebra. The fundamental representation of SU(3) spin operators T^μ (for $\mu = 1, \dots, 8$) can be constructed as

$$T^7 = +S^x, \tag{S1a}$$

$$T^5 = -S^y, \tag{S1b}$$

$$T^2 = +S^z, \tag{S1c}$$

$$T^3 = -[(S^x)^2 - (S^y)^2], \tag{S1d}$$

$$T^8 = -\frac{1}{\sqrt{3}}[(S^x)^2 + (S^y)^2 - 2(S^z)^2], \tag{S1e}$$

* These authors contributed equally.

† chenxray@pku.edu.cn

$$T^1 = -[S^x S^y + S^y S^x], \quad (\text{S1f})$$

$$T^4 = -[S^x S^z + S^z S^x], \quad (\text{S1g})$$

$$T^6 = -[S^y S^z + S^z S^y]. \quad (\text{S1h})$$

where $\mathbf{S} = (S^x, S^y, S^z)$ are spin-1 dipole moments that satisfy the SU(2) commutation relation $[S^\alpha, S^\beta] = \iota \epsilon_{\alpha\beta\gamma} S^\gamma$, where $\epsilon_{\alpha\beta\gamma}$ denotes the antisymmetric tensor. The later five operators with the bilinear form describe the quadrupole moments as introduced in the main text

$$\mathbf{Q} = (Q^{x^2-y^2}, Q^{r^2-3z^2}, Q^{xy}, Q^{zx}, Q^{yz}) = -(T^3, T^8, T^1, T^4, T^6). \quad (\text{S2})$$

Since they comprise the fundamental representation of $\mathfrak{su}(3)$ Lie algebra, T^μ are traceless Hermitian matrices and satisfy the orthonormality condition

$$\text{Tr}(T^\alpha T^\beta) = 2\delta_{\alpha\beta}, \quad (\text{S3})$$

and the commutation relations

$$[T^\alpha, T^\beta] = \iota f_{\alpha\beta\gamma} T^\gamma. \quad (\text{S4})$$

Note that a summation over repeated Greek indices is supposed hereafter unless otherwise specified. The factors $f_{\alpha\beta\gamma}$ are known as structure constants, which can be defined by the Gell-Mann matrices λ_μ as

$$f_{\eta\mu\nu} = -\frac{\iota}{2} \text{Tr}(\lambda_\eta [\lambda_\mu, \lambda_\nu]). \quad (\text{S5})$$

With this representation, one can prove the identity

$$\mathbf{Q}_i \cdot \mathbf{Q}_j = 2(\mathbf{S}_i \cdot \mathbf{S}_j)^2 + \mathbf{S}_i \cdot \mathbf{S}_j - \frac{2}{3} S^2 (S+1)^2, \quad (\text{S6})$$

and recast the BBQ Hamiltonian \mathcal{H} with the SU(3) spin operators T^μ as Equation (2) in the main text.

In terms of the Cartesian basis $|\alpha\rangle$ ($\alpha = x, y, z$), it is more transparent that the spin operators T^μ are generators of the Lie algebra associated to the SU(3)

$$\langle \alpha | T^\mu | \beta \rangle = (\lambda_\mu)_{\alpha\beta}, \quad (\text{S7})$$

and an arbitrary spin-1 state at site i can be expressed as a linear combination $|\mathbf{Z}_i\rangle = Z_i^\alpha |\alpha\rangle_i$ where $\mathbf{Z}_i = (Z_i^x, Z_i^y, Z_i^z)^\top$ is a three-dimensional complex vector. After considering the normalization condition, a physical SU(3) coherent state

$$|\mathbf{\Omega}\rangle = \frac{1}{2}(1 + \cos \vartheta) \exp(-\iota\varphi) |1\rangle + \frac{1}{\sqrt{2}} |0\rangle + \frac{1}{2}(1 - \cos \vartheta) \exp(+\iota\varphi) |\bar{1}\rangle \quad (\text{S8})$$

takes the value on a complex projective space given by the quotient group $S^5/S^1 \cong S^5/U(1) \cong \mathbb{C}P^2$. The expectation values of SU(3) spin operators in the coherent states define the color fields

$$n_i^\mu = \langle \mathbf{Z}_i | T_i^\mu | \mathbf{Z}_i \rangle = \mathbf{Z}_i^\dagger \lambda_\mu \mathbf{Z}_i. \quad (\text{S9})$$

Under the semiclassical SU(3) approximation, the variational energy of the system is given by

$$H_v = \langle \mathbf{Z} | \mathcal{H} | \mathbf{Z} \rangle = \sum_{\langle ij \rangle} J |\mathbf{Z}_i^\dagger \cdot \mathbf{Z}_j|^2 - (J+K) |\mathbf{Z}_i \cdot \mathbf{Z}_j|^2 + D_z \sum_i |Z_i^z|^2 = \sum_{\langle ij \rangle} \mathcal{J}^\mu n_i^\mu n_j^\mu - \frac{D_z}{\sqrt{3}} \sum_i n_i^8, \quad (\text{S10})$$

where $\mathcal{J}^\mu = (J + K/2)(\delta_{\mu 7} + \delta_{\mu 5} + \delta_{\mu 2}) - K/2(\delta_{\mu 3} + \delta_{\mu 8} + \delta_{\mu 1} + \delta_{\mu 4} + \delta_{\mu 6})$. For the sake of efficiency, we first determine the number of degrees of freedom (DOF) in the $\mathbb{C}P^2$ space on each site. A free complex vector \mathbf{Z}_i with three components can be generically parameterized by six variables, but the normalization condition $\mathbf{Z}_i^\dagger \cdot \mathbf{Z}_i = 1$ indicates a redundant global phase. The color field also satisfies following constraints $n^\mu n^\mu = \frac{4}{3}$ and $n^\mu = \frac{3}{2} d_{\mu\nu\eta} n^\nu n^\eta$, where $d_{\mu\nu\eta} = \frac{1}{4} \text{Tr}(\lambda_\mu \{\lambda_\nu, \lambda_\eta\})$ are the symmetric symbols of SU(3). The combination of above relations lead to the Casimir identity $d_{\mu\nu\eta} n^\mu n^\nu n^\eta = 8/9$, which further reduces the number of DOF to four.

At this stage, we can safely parameterize \mathbf{Z}_i or n_i^μ in four independent variables at each site and conduct the optimization procedures for H_v on an $L \times L$ superlattice with the periodic boundary conditions via the NLOpt nonlinear optimization package [1]. The superlattice size is taken from $L = 1$ to 6. The optimization is repeated at least 128 times for each geometry with randomly initialized spin configurations. In all cases, the lowest energy is unique within the numerical error. Inspired by the numerical results, we further refine the ground-state configurations by taking a set of parameters with a minimum number to obtain analytic descriptions. Besides the FQ phase, three phases with non-zero $\langle \mathbf{S} \rangle$ are identified and parameterized in Tables I, II, and III, whose boundaries are presented in Fig. 1(a) of the main text.

A. The pure FQ phase

For $J/K > 2$, a pure FQ phase is always favored at the level of the semiclassical SU(3) approximation. In the generic case where $D_z > 0$, the optimized complex vectors \mathbf{Z}_i are

site-independent

$$\mathbf{Z}_i = [\cos \phi, \sin \phi, 0], \quad (\text{S11})$$

where ϕ is determined by the interaction parameters $(K, D_z)/J$. The wavefunction of the pure FQ phase is given by the direct product $|\Psi\rangle = \prod_i |\mathbf{Z}_i\rangle$ where $|\mathbf{Z}_i\rangle = \cos \phi |x\rangle_i + \sin \phi |y\rangle_i$. It is easy to verify the vanishing of dipole components $\langle S_i^\alpha \rangle = 0$. The non-zero quadruple moments are

$$-Q_i^{x^2-y^2} = \cos 2\phi, \quad -Q_i^{r^2-3z^2} = \frac{1}{\sqrt{3}}, \quad -Q_i^{xy} = \sin 2\phi, \quad (\text{S12})$$

Note that the expectation of $Q^{r^2-3z^2}$ is a constant due to the polarization effect from the single-ion anisotropy term $(S_i^z)^2$ when $D_z > 0$.

B. The coexistence phases

The first phase, labeled by I, can be quantitatively parameterized based on the numerical optimization results. For convenience, the S^y component is fixed to be zero hereafter to eliminate the ambiguity due to the U(1) degeneracy on the x - y plane in spin space. The three complex vectors on a triangular plaquette are given by

$$\mathbf{Z}_1 = \frac{1}{\sqrt{2}}[(1 + \iota) \cos \phi_1, -(1 - \iota) \sin \phi_1, 0], \quad (\text{S13})$$

$$\mathbf{Z}_2 = \frac{1}{\sqrt{2}}[(1 + \iota) \sin \theta \cos \phi_2, (1 - \iota) \sin \theta \sin \phi_2, (1 + \iota) \cos \theta], \quad (\text{S14})$$

$$\mathbf{Z}_3 = \frac{1}{\sqrt{2}}[-(1 + \iota) \sin \theta \cos \phi_2, -(1 - \iota) \sin \theta \sin \phi_2, (1 + \iota) \cos \theta], \quad (\text{S15})$$

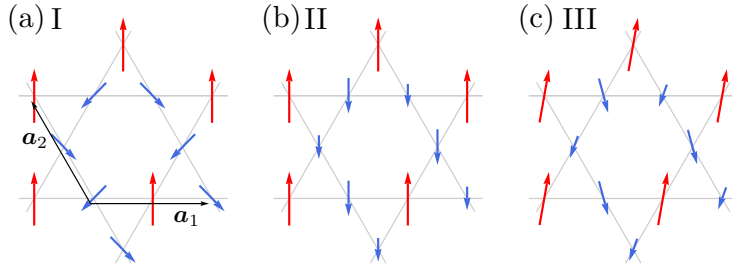


FIG. S1. The dipole spin configurations for the coexistence phases. In all phases, each triangular plaquette hosts three different single-site states with distinct orders, inducing an extensive ground-state degeneracy. Major dipolar spins vectors are highlighted in red.

where θ and $\phi_{1,2}$ are dependent on $(K, D_z)/J$. The explicit forms for eight spin components are listed in Table I. We first focus on the dipole moments. In the particular case where $D_z = 0$, one has $\tan \phi_2 = 2 \tan \phi_1$ and $\sqrt{3} \tan \theta \cos \phi_2 = 1$, leading to a 120° clock configuration for dipolar components $\langle \mathbf{S}_i \rangle$ with a uniform but reduced length $|\mathbf{S}_i| = \sin^2 2\phi_1$ satisfying $\sum_{i \in \text{tri}} \langle \mathbf{S}_i \rangle = 0$. The presence of D_z immediately introduces a finite net magnetization on each triangular plaquette to gain energy from the $(S_i^z)^2$ term. As a consequence, two of the three vectors \mathbf{S}_i acquire a further reduced length, and their directions become more closer to the z -axis in spin space, albeit they are still antiparallel to the major one. This configuration is depicted in Fig. S1(a). Quantitatively, the full dipole components can be decomposed into two parts

$$\sum_{i \in \text{tri}} \langle \mathbf{S}_i \rangle = 3\mathbf{S}_{\text{FM}} + \sum_{i \in \text{tri}} \langle \mathbf{S}'_i \rangle, \quad (\text{S16})$$

where the FM part is

$$\mathbf{S}_{\text{FM}} = \left(0, 0, \frac{1}{3} \sin 2\phi_1 - \frac{2}{3} \sin^2 \theta \sin 2\phi_2 \right). \quad (\text{S17})$$

The rest part serves as a local constraint on each triangular plaquette

$$\sum_{i \in \text{tri}} \langle \mathbf{S}'_i \rangle = 0. \quad (\text{S18})$$

This decomposition is intuitively depicted in Fig. S2(a). Note that there are two types of configurations on one triangular plaquette from the complex vectors \mathbf{Z}_i . They are related by the time-reversal symmetry and thus characterized by opposite signs of \mathbf{S}_{FM} . Once imposed on the entire lattice, only one of them can appear in a given ground-state configuration because of the local constraint. Therefore, the magnetization is uniform on every triangular plaquette, resulting in a global spontaneous breaking of time-reveal symmetry and an additional Z_2 degeneracy.

In one-to-one correspondence with the three different dipole components $\langle \mathbf{S}_i \rangle$, there are three different quadrupole components $\langle \mathbf{Q}_i \rangle$ as listed in Table I. An FQ part can be separated from each triangular plaquette in a similar form

$$\sum_{i \in \text{tri}} \langle \mathbf{Q}_i \rangle = 3\mathbf{Q}_{\text{FQ}} + \sum_{i \in \text{tri}} \langle \mathbf{Q}'_i \rangle, \quad (\text{S19})$$

where

$$\mathbf{Q}_{\text{FQ}} = \left(\frac{1}{3} \cos 2\phi_1 + \frac{2}{3} \sin^2 \theta \cos 2\phi_2, \frac{-1}{\sqrt{3}} \cos 2\theta, 0, 0, 0 \right). \quad (\text{S20})$$

TABLE I. The spin configuration on the triangular plaquette for dipolar and quadrupolar DOF in phase I. The parameters θ and $\phi_{1,2}$ are dependent on $(K, D_z)/J$. The S^y component has been fixed to zero for convenience.

	S^x	$-S^y$	S^z	$-Q^{x^2-y^2}$	$-Q^{r^2-3z^2}$	$-Q^{xy}$	$-Q^{zx}$	$-Q^{yz}$
1	0	0	$\sin 2\phi_1$	$\cos 2\phi_1$	$\frac{1}{\sqrt{3}}$	0	0	0
2	$+\sin 2\theta \sin \phi_2$	0	$-\sin^2 \theta \sin 2\phi_2$	$\sin^2 \theta \cos 2\phi_2$	$\frac{1}{\sqrt{3}}(1 - 3\cos^2 \theta)$	0	$+\sin 2\theta \cos \phi_2$	0
3	$-\sin 2\theta \sin \phi_2$	0	$-\sin^2 \theta \sin 2\phi_2$	$\sin^2 \theta \cos 2\phi_2$	$\frac{1}{\sqrt{3}}(1 - 3\cos^2 \theta)$	0	$-\sin 2\theta \cos \phi_2$	0

The rest part also serves as a local constraint but for the quadrupole moments

$$\sum_{i \in \text{tri}} \langle \mathbf{Q}'_i \rangle = 0. \quad (\text{S21})$$

A schematic plot of this decomposition is shown in Fig. S2(b) for comparison. In this channel, the time-reversal symmetry is always preserved. The two local constraints for $\langle \mathbf{S}' \rangle$ and $\langle \mathbf{Q}' \rangle$ are the hallmark of classical spin liquids and responsible for the extensive ground-state degeneracy. One can thus regard the ground state as a composite of a classical spin liquid and ferroicities for both dipolar and quadrupolar DOFs.

The rest two phases can be understood in a similar manner. The phase II, parameterized in Table II, appears when D_z/J is large enough. By refining the numerical results, the spin configurations can be quantitatively described by

$$\mathbf{Z}_i = \frac{1}{\sqrt{2}}(\cos \phi_i + \imath \cos \phi_i, -\sin \phi_i + \imath \sin \phi_i, 0). \quad (\text{S22})$$

Because of the significant energy gain from the strong single-ion anisotropy, the dipolar DOF on every site are parallel/antiparallel along the z direction in spin space. Specifically, all three dipole moments have nonequivalent expectation values as shown in Fig. S1(b) where the major dipole spins with the largest $\langle \mathbf{S} \rangle$ are highlighted in red. The rest two spins with smaller lengths are in the opposite direction of the major one. In the quadrupole channel, only $Q^{x^2-y^2}$ and $Q^{r^2-3z^2}$ have non-zero expectations (once the S^y component is fixed to be zero), and the latter is a constant on all sublattices.

The last phase, III, is sandwiched between phases I and II when $K/J \lesssim 0.243$ and can

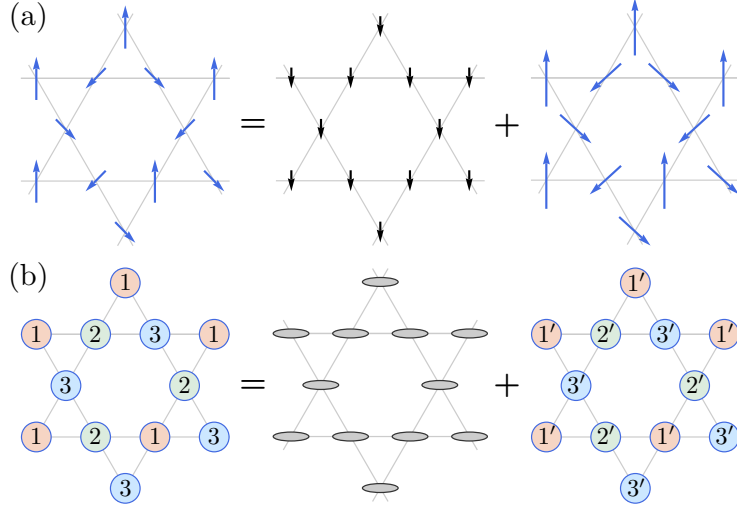


FIG. S2. The decompositions of (a) dipole and (b) quadrupole spin components for phase I with a finite easy-axis anisotropy D_z . There are three different vectors $\langle \mathbf{S}_i \rangle$ ($\langle \mathbf{Q}_i \rangle$) on the triangular plaquette, in which a uniform FM (FQ) part can be separated. The rest part satisfies the constraint $\sum_{i \in \text{tri}} \langle \mathbf{S}'_i \rangle = 0$ ($\sum_{i \in \text{tri}} \langle \mathbf{Q}'_i \rangle = 0$), indicating the classical-spin-liquid physics. The FM part vanishes in the isotropic limit where $D_z = 0$.

be parameterized in Table III and defined by the complex vectors

$$\mathbf{Z}_i = \frac{1}{\sqrt{2}} [-(1 + \nu) \sin \theta_i \cos \phi_i, -(1 - \nu) \sin \theta_i \sin \phi_i, (1 + \nu) \cos \theta_i]. \quad (\text{S23})$$

As shown in the inset of Fig. S1(c), it has a more odd configuration with a lower symmetry for dipole moments. Compared with phase II, the dipolar components \mathbf{S}_i in phase III can be viewed as rotations from the colinear order along a fixed direction but at different angles on different sublattices. Based on the same reason explained for phase I, phases II and III can

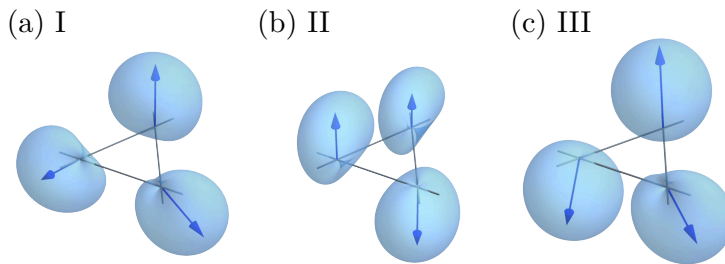


FIG. S3. The probability amplitudes $|\langle \boldsymbol{\Omega} | \mathbf{Z} \rangle|^2$ on the triangular plaquette for (a) phase I with $(K, D_z)/J = (1.0, 1.0)$, (b) phase II with $(K, D_z)/J = (1.0, 2.5)$, and (c) phase III with $(K, D_z)/J = (0.1, 2.3)$. The spin configuration for dipolar DOF $\langle \mathbf{S}_i \rangle$ are indicated by blue arrows.

TABLE II. The spin configuration on the triangular plaquette for dipolar and quadrupolar DOF in phase II. The parameters $\phi_{1,2,3}$ are dependent on $(K, D_z)/J$. The S^y component has been fixed to zero for convenience.

	S^x	$-S^y$	S^z	$-Q^{x^2-y^2}$	$-Q^{r^2-3z^2}$	$-Q^{xy}$	$-Q^{zx}$	$-Q^{yz}$
1	0	0	$\sin 2\phi_1$	$\cos 2\phi_1$	$\frac{1}{\sqrt{3}}$	0	0	0
2	0	0	$\sin 2\phi_2$	$\cos 2\phi_2$	$\frac{1}{\sqrt{3}}$	0	0	0
3	0	0	$\sin 2\phi_3$	$\cos 2\phi_3$	$\frac{1}{\sqrt{3}}$	0	0	0

TABLE III. The spin configuration on the triangular plaquette for dipolar and quadrupolar DOF in phase III. The parameters $\theta_{1,2,3}$ and $\phi_{1,2,3}$ are dependent on $(K, D_z)/J$. The S^y component has been fixed to zero for convenience.

	S^x	$-S^y$	S^z	$-Q^{x^2-y^2}$	$-Q^{r^2-3z^2}$	$-Q^{xy}$	$-Q^{zx}$	$-Q^{yz}$
1	$-\sin 2\theta_1 \sin \phi_1$	0	$-\sin^2 \theta_1 \sin 2\phi_1$	$\sin^2 \theta_1 \cos 2\phi_1$	$\frac{1}{\sqrt{3}}(1 - 3 \cos^2 \theta_1)$	0	$-\sin 2\theta_1 \cos \phi_1$	0
2	$-\sin 2\theta_2 \sin \phi_2$	0	$-\sin^2 \theta_2 \sin 2\phi_2$	$\sin^2 \theta_2 \cos 2\phi_2$	$\frac{1}{\sqrt{3}}(1 - 3 \cos^2 \theta_2)$	0	$-\sin 2\theta_2 \cos \phi_2$	0
3	$-\sin 2\theta_3 \sin \phi_3$	0	$-\sin^2 \theta_3 \sin 2\phi_3$	$\sin^2 \theta_3 \cos 2\phi_3$	$\frac{1}{\sqrt{3}}(1 - 3 \cos^2 \theta_3)$	0	$-\sin 2\theta_3 \cos \phi_3$	0

also be decomposed in both dipole and quadruple channel and be regarded as a composite of a classical spin liquid and ferroicities for both dipolar and quadrupolar DOFs. To be more visual, Fig. S3 presents the probability amplitudes $|\langle \mathbf{\Omega} | \mathbf{Z} \rangle|^2$ by projecting the ground states on the SU(3) spin coherent state $|\mathbf{\Omega}\rangle$.

II. FLAVOR WAVE THEORY AND EXCITATIONS

Since the FQ phase is well ordered, it is a good starting point to consider its instability towards the phases with $\langle \mathbf{S} \rangle \neq 0$ under the quantum fluctuations. For this purpose, we associate three Schwinger bosons $b_{i\alpha}^\dagger$ ($b_{i\alpha}$) with $\alpha = x, y, z$ at each site to create (annihilate) the three time-reversal invariant basis as

$$b_{i\alpha}^\dagger |\emptyset\rangle \equiv |\alpha\rangle, \quad (\alpha = x, y, z). \quad (\text{S24})$$

In terms of three flavors of Schwinger bosons, the dipole and quadrupole operators are given by

$$S_i^\alpha = -i\varepsilon_{\alpha\beta\gamma} b_{i\beta}^\dagger b_{i\gamma}, \quad (\text{S25a})$$

$$Q_i^{x^2-y^2} = -b_{ix}^\dagger b_{ix} + b_{iy}^\dagger b_{iy}, \quad (\text{S25b})$$

$$Q_i^{x^2-3z^2} = (2b_{iz}^\dagger b_{iz} - b_{ix}^\dagger b_{ix} - b_{iy}^\dagger b_{iy})/\sqrt{3}, \quad (\text{S25c})$$

$$Q_i^{xy} = -b_{ix}^\dagger b_{iy} - b_{iy}^\dagger b_{ix}, \quad (\text{S25d})$$

$$Q_i^{yz} = -b_{iy}^\dagger b_{iz} - b_{iz}^\dagger b_{iy}, \quad (\text{S25e})$$

$$Q_i^{zx} = -b_{iz}^\dagger b_{ix} - b_{ix}^\dagger b_{iz}. \quad (\text{S25f})$$

This representation enlarges the fundamental representation at each site and we need to reinstate the physical Hilbert space by imposing a single occupancy constraint

$$\sum_{\alpha=x,y,z} b_{i\alpha}^\dagger b_{i\alpha} = 1. \quad (\text{S26})$$

The Hamiltonian in Eq. (2) of the main text can be re-expressed in terms of the Schwinger bosons

$$H_{\text{FW}} = \sum_{\langle ij \rangle} J b_{i\alpha}^\dagger b_{j\alpha} b_{j\beta}^\dagger b_{i\beta} - (J + K) b_{i\alpha}^\dagger b_{j\alpha}^\dagger b_{j\beta} b_{i\beta} + D_z \sum_i b_{iz}^\dagger b_{iz}, \quad (\text{S27})$$

where the repeated Greek indices should be summarized over three flavors.

Without loss of generality, it is assumed that the flavor x of Schwinger bosons is condensed at each site in the FQ phase via the following substitution

$$b_{i,x}^\dagger = b_{i,x} = \sqrt{1 - b_{i,y}^\dagger b_{i,y} - b_{i,z}^\dagger b_{i,z}} \approx 1 - \frac{1}{2}(b_{i,y}^\dagger b_{i,y} + b_{i,z}^\dagger b_{i,z}). \quad (\text{S28})$$

The rest two flavors now play the roles of Holstein-Primakoff bosons and characterize the quantum fluctuations on the y - z plane. After this substitution and the Fourier transformation

$$b_{i\alpha} = \frac{1}{\sqrt{N}} \sum_{\mathbf{k}} e^{-i\mathbf{k}\cdot\mathbf{r}_i} b_{\mathbf{k}\alpha}, \quad b_{i\alpha}^\dagger = \frac{1}{\sqrt{N}} \sum_{\mathbf{k}} e^{+i\mathbf{k}\cdot\mathbf{r}_i} b_{\mathbf{k}\alpha}^\dagger, \quad (\text{S29})$$

where N is the number of sites, The Hamiltonian H_{FW} could be further recast into the bosonic Bogoliubov-de-Gennes (BdG) form in reciprocal space

$$H(\mathbf{k}) = \begin{pmatrix} \psi_{\mathbf{k}}^\dagger & \psi_{-\mathbf{k}} \end{pmatrix} \begin{pmatrix} A_{\mathbf{k}} + C & B_{\mathbf{k}} \\ B_{\mathbf{k}}^\dagger & A_{-\mathbf{k}}^* + C \end{pmatrix} \begin{pmatrix} \psi_{\mathbf{k}} \\ \psi_{-\mathbf{k}}^\dagger \end{pmatrix}, \quad (\text{S30})$$

with the basis $\psi_{\mathbf{k}}^\dagger = (b_{\mathbf{k}1y}^\dagger, b_{\mathbf{k}2y}^\dagger, b_{\mathbf{k}3y}^\dagger, b_{\mathbf{k}1z}^\dagger, b_{\mathbf{k}2z}^\dagger, b_{\mathbf{k}3z}^\dagger)$. The number index labels three sublattices. The blocked matrix elements read $A_{\mathbf{k}} = J\mathbb{I}_2 \otimes \mathcal{M}_{\mathbf{k}}$, $B_{\mathbf{k}} = -(J + K)\mathbb{I}_2 \otimes \mathcal{M}_{\mathbf{k}}$, and $C = 2K\mathbb{I}_6 + \frac{1}{2}D_z \text{diag}(0, 1) \otimes \mathbb{I}_3$ where

$$\mathcal{M}_{\mathbf{k}} = \begin{pmatrix} 0 & \cos \frac{\mathbf{k} \cdot \mathbf{a}_1}{2} & \cos \frac{\mathbf{k} \cdot (\mathbf{a}_1 + \mathbf{a}_2)}{2} \\ \cos \frac{\mathbf{k} \cdot \mathbf{a}_1}{2} & 0 & \cos \frac{\mathbf{k} \cdot \mathbf{a}_2}{2} \\ \cos \frac{\mathbf{k} \cdot (\mathbf{a}_1 + \mathbf{a}_2)}{2} & \cos \frac{\mathbf{k} \cdot \mathbf{a}_2}{2} & 0 \end{pmatrix}. \quad (\text{S31})$$

We have introduced the lattice vectors $\mathbf{a}_1 = (1, 0)$ and $\mathbf{a}_2 = (-1/2, \sqrt{3}/2)$ for the pristine kagomé lattice. The bosonic BdG Hamiltonian $H(\mathbf{k})$ can be diagonalized under the paraunitary or Krein-unitary transformation with $(\psi_{\mathbf{k}}^\dagger, \psi_{-\mathbf{k}}) \mathcal{U}^\dagger(\mathbf{k}) = (\beta_{\mathbf{k}}^\dagger, \beta_{-\mathbf{k}})$ where $\beta_{\mathbf{k}}^\dagger = (\beta_{\mathbf{k}1y}^\dagger, \beta_{\mathbf{k}2y}^\dagger, \beta_{\mathbf{k}3y}^\dagger, \beta_{\mathbf{k}1z}^\dagger, \beta_{\mathbf{k}2z}^\dagger, \beta_{\mathbf{k}3z}^\dagger)$. The standard diagonalization procedure leads to

$$H(\mathbf{k}) = \sum_{\mathbf{k}} \sum_{m=1}^3 \omega_{m\alpha}(\mathbf{k}) \beta_{\mathbf{k}m\alpha}^\dagger \beta_{\mathbf{k}m\alpha} + \omega_{m\alpha}(-\mathbf{k}) \beta_{-\mathbf{k}m\alpha} \beta_{-\mathbf{k}m\alpha}^\dagger, \quad (\text{S32})$$

where the dispersions of the linear flavor wave (LFW) excitations are given by

$$\omega_1(\mathbf{k}) = [3K(K - 2J)]^{1/2}, \quad (\text{S33})$$

$$\omega_2(\mathbf{k}) = [(6K + D_z)(2K + D_z - 4J)]^{1/2}, \quad (\text{S34})$$

$$\omega_{3,4}(\mathbf{k}) = \left[3K^2 - (2J + K)KF(\mathbf{k})/2 \pm (K - 2J)/K/2\sqrt{3 + 2F(\mathbf{k})} \right]^{1/2}, \quad (\text{S35})$$

$$\omega_{5,6}(\mathbf{k}) = \left[D_z^2/4 + D_z J/2 + 2D_z K + 3K^2 - K(J + K/2)F(\mathbf{k}) \right. \\ \left. \pm (D_z J + 2JK - K^2)/2\sqrt{3 + 2F(\mathbf{k})} \right]^{1/2}. \quad (\text{S36})$$

The lattice structure factor $F(\mathbf{k}) = \cos(\mathbf{k} \cdot \mathbf{a}_1) + \cos(\mathbf{k} \cdot \mathbf{a}_2) + \cos[\mathbf{k} \cdot (\mathbf{a}_1 + \mathbf{a}_2)]$ has been introduced.

Because the single-ion anisotropy term is only associated with the z flavor, half of the branches of spin excitations are independent of the parameter D_z in the LFW theory. As shown in Figs.2 (a) and (d) of the main text, there is a gapless mode at the Γ point corresponding to the Nambu-Goldstone bosons. This mode appears necessarily in an FQ ground state due to the spontaneous breaking of the U(1) continuous symmetry. In addition, there are two flat bands with eigenvalues

$$\omega_1(\mathbf{k}) = \sqrt{3K(K - 2J)}, \quad (\text{S37})$$

$$\omega_2(\mathbf{k}) = \sqrt{(6K + D_z)(2K + D_z - 4J)}, \quad (\text{S38})$$

respectively. The first is non-negative in the FQ phase and decreases with the biquadratic interaction K/J . It becomes zero at the phase boundary where $K/J = 2$ and unphysical once $K/J < 2$, indicating the instability of the FQ phase. This D_z -independent instability is fully consistent with the semi-classical phase boundary shown in Fig. 1(a) of the main text.

To elucidate the impact of quantum fluctuations, we calculate the dynamical SSFs in both dipolar and quadrupolar channels

$$\mathcal{S}^{\text{LFW}}(\mathbf{q}, \omega) = \int_{-\infty}^{+\infty} \frac{dt}{2\pi} e^{i\omega t} \langle \mathbf{S}_{\mathbf{q}}(t) \cdot \mathbf{S}_{-\mathbf{q}}(0) \rangle, \quad (\text{S39})$$

$$\mathcal{Q}^{\text{LFW}}(\mathbf{q}, \omega) = \int_{-\infty}^{+\infty} \frac{dt}{2\pi} e^{i\omega t} \langle \mathbf{Q}_{\mathbf{q}}(t) \cdot \mathbf{Q}_{-\mathbf{q}}(0) \rangle. \quad (\text{S40})$$

Note that $S_i^x S_j^x$ and $Q_i^{yz} Q_j^{yz}$ do not contribute to dynamical SSFs at the LFW level because the preset nematic director \mathbf{Z} is parallel to the x axis. The results with a logarithmic rescale for $\mathcal{Q}^{\text{LFW}}(\mathbf{q}, \omega)$ are displayed in the second and third rows of Fig. 2. Our analysis reveals that the dynamical SSFs on two flat bands are almost entirely contributed by the dipolar DOF. With the decreasing of K/J , the dynamical SSFs in the dipolar channel $\mathcal{S}^{\text{LFW}}(\mathbf{q}, \omega)$ drastically redistribute and gradually concentrate on the lowest flat band $\omega_1(\mathbf{k})$, especially near the momentum \mathbf{K} , as shown in Fig. 2(e). However, such a broad peak cannot be regarded as a precursor of the conventional 3-sublattice antiferromagnetic order. The failure of this dipolar ordering is more transparent in the static SSF $\mathcal{S}^{\text{LFW}}(\mathbf{q}, \omega = 0)$ shown in Fig. S4(a). The static SSF for the flat band $\omega_1(\mathbf{k}) = 0$ on the phase boundary clearly exhibits a pinch point singularities in the dipolar channel, which is reminiscent of those observed in the Coulomb liquid phase of kagomé spin ice [2–4]. Meanwhile, the equal-time SSFs

$$\mathcal{Q}^{\text{LFW}}(\mathbf{q}) = \int d\omega \mathcal{Q}^{\text{LFW}}(\mathbf{q}, \omega), \quad (\text{S41})$$

in the quadrupolar channel are still dominated by the FQ correlations characterized by the divergent peak at $\mathbf{\Gamma}$ point. Although the pinch-point singularities in static SSF $\mathcal{S}^{\text{LFW}}(\mathbf{q}, \omega = 0)$ may not align with a real classical spin liquid due to the vanished expectation $\langle \mathbf{S} \rangle$ at the FQ phase boundary where the LFW results are already instable, these findings still light on the possibility of the coexistence of a classical spin liquid and long-rang orders from different DOF after the phase transition.

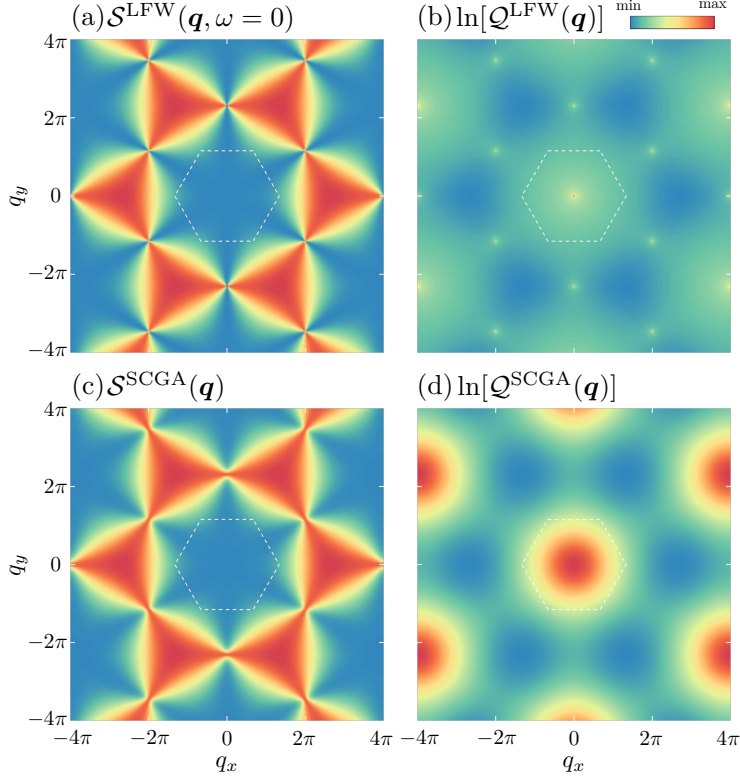


FIG. S4. (a-b) SSFs from the LFW theory at the FQ phase boundary $(K_c, D_z)/J = (2.0, 1.0)$ where $\omega_1(\mathbf{k}) = 0$. The dipolar static SSF $\mathcal{S}^{\text{LFW}}(\mathbf{q})$ on the flat band exhibits pinch-point-like pattern. The quadrupolar equal-time SSF $\mathcal{Q}^{\text{LFW}}(\mathbf{q})$ displayed in a logarithmic scale shows a divergent peak at Γ point. (c-d) SSFs from the SCGA theory in the phase I with $(K, D_z) = (1.0, 1.0)$ at $T/J = 0.1$. The dashed-line hexagon indicates the first Brillouin zone.

III. SPIN CORRELATION FROM SCGA

In parallel to the optimizations of ground-state energy, one can directly calculate the spin correlations at finite temperatures via the self-consistent Gaussian approximation (SCGA) under the local Hilbert-space constraint

$$|\langle \mathbf{T}_i \rangle|^2 = |\langle \mathbf{Z}_i | \mathbf{S}_i | \mathbf{Z}_i \rangle|^2 + |\langle \mathbf{Z}_i | \mathbf{Q}_i | \mathbf{Z}_i \rangle|^2 = \frac{4}{3}, \quad (\text{S42})$$

which can be verified by the definition of color fields in Eq. (S9). In this framework, the partition function of the spin-1 system in Eq. (2) of the main text can be expressed as

$$\mathcal{Z} = \int \mathcal{D}[\mathbf{T}, \lambda] e^{-\beta H + \sum_i \lambda_i (\mathbf{T}_i^2 - \frac{4}{3})} \approx \int \mathcal{D}[\mathbf{T}, \lambda] e^{-\mathcal{S}_{\text{eff}}[\beta, \lambda_i]}, \quad (\text{S43})$$

where an auxiliary field λ_i has been introduced as Lagrange multipliers to enforce the local Hilbert-space constraint stated in Eq. (S42) and β is the inverse of temperature. At high temperatures, the fluctuation of the auxiliary field should become negligible and all lattice symmetries are expected to be restored. We thus perform a saddle point approximation to seek states that respect the local Hilbert-space constraint in the form of a global average $\lambda_i = -\beta\Delta(T)$ where $\Delta(T)$ is a purely real number. This yields an effective action

$$\begin{aligned}\mathcal{S}_{\text{eff}} &= \beta \sum_{\mathbf{k}} \mathbf{T}_{\mathbf{k}} [\mathcal{J}(\mathbf{k}) + \Delta(T) \otimes \mathbb{I}_{24}] \mathbf{T}_{-\mathbf{k}} - 4\beta N \Delta(T) \\ &= \beta \sum_{\mathbf{k}} \sum_{mn}^3 T_{\mathbf{k}m}^{\mu} [\mathcal{J}_{mn}^{\mu}(\mathbf{k}) + \Delta(T) \delta_{mn}] T_{-\mathbf{k}n}^{\mu} - 4\beta N \Delta(T),\end{aligned}\quad (\text{S44})$$

where $\mathbf{T}_{\mathbf{k}m} = \frac{1}{\sqrt{N}} \sum_{\mathbf{r}} T_{r m} e^{+i\mathbf{k}\cdot\mathbf{r}}$ is the Fourier transformation of spin components and N is the number of unit cells. The indices \mathbf{r} and m are the position of unit cell and label of sublattice, respectively. The matrices $\mathcal{J}(\mathbf{k})$ are block-diagonalized in spin component space

$$\mathcal{J}^{\mu}(\mathbf{k}) = \begin{cases} (J + K/2)\mathbf{J}(\mathbf{k}) - D_z \mathbb{I}_3 \delta_{2\mu} & \mu = 7, 5, 2 \\ -K/2\mathbf{J}(\mathbf{k}) & \mu = 3, 1, 4, 6, 8 \end{cases} \quad (\text{S45})$$

where $\mathbf{J}(\mathbf{k})$ is a 3×3 matrix

$$\mathbf{J}(\mathbf{k}) = \begin{pmatrix} 0 & \cos \frac{\mathbf{k}\cdot\mathbf{a}_1}{2} & \cos \frac{\mathbf{k}\cdot(\mathbf{a}_1+\mathbf{a}_2)}{2} \\ \cos \frac{\mathbf{k}\cdot\mathbf{a}_1}{2} & 0 & \cos \frac{\mathbf{k}\cdot\mathbf{a}_2}{2} \\ \cos \frac{\mathbf{k}\cdot(\mathbf{a}_1+\mathbf{a}_2)}{2} & \cos \frac{\mathbf{k}\cdot\mathbf{a}_2}{2} & 0 \end{pmatrix}. \quad (\text{S46})$$

The correlation functions between spin components \mathbf{T}_i can be readily obtained

$$\langle T_{\mathbf{k}m}^{\mu} T_{-\mathbf{k}n}^{\nu} \rangle = \frac{1}{2\beta} [\mathcal{J}(\mathbf{k}) + \Delta(T) \otimes \mathbb{I}_{24}]_{\mu\nu, mn}^{-1}. \quad (\text{S47})$$

The saddle point parameter $\Delta(T)$ is determined self-consistently from the saddle point equation

$$\frac{1}{N} \sum_{\mathbf{k}} \sum_{\mu, m} \frac{1}{2\beta} [\mathcal{J}(\mathbf{k}) + \Delta(T) \mathbb{I}_{24}]_{\mu\mu, mm}^{-1} = 4. \quad (\text{S48})$$

In Figs. S4(b) and (c), we preset the static SSFs $\mathcal{S}^{\text{SCGA}}(\mathbf{q})$ and $\mathcal{Q}^{\text{SCGA}}(\mathbf{q})$ for dipole and quadrupole moments in phase I, respectively. Clearly, the dipolar SSF exhibits a pinch-point pattern as the one obtained from the LFW theory at the FQ boundary, although

the singularities at $2\mathbf{M}$ points disappear because of the thermal broadening. The effect of thermal fluctuations is more significant in the quadrupolar channel. Compared with Fig. S4(b), the peak of FQ order at Γ point is melted into a hump, indicating a quasi-long-range order at finite temperatures.

Although the features of the classical spin liquid and FQ order can be identified in SSFs obtained by the SCGA method, there is no signal of the predicted FM order in the dipolar channel even at $T/J = 0.1$. The pinch-point pattern of the coexisting classical spin liquid is also missing in the the quadrupolar SSFs. In fact, the spin components T_i^μ in the SCGA method are treated as Gaussian variables that are merely subject to a relaxed global constraint. In contrast to the optimization in $\mathbb{C}P^2$ space, the nontrivial independency inherited from the $\mathfrak{su}(3)$ Lie algebra can not be captured by the SCGA method. To correctly reveal the finite-temperature properties of spin correlations in the coexistence phases, we perform the semiclassical Mento Carlo (sMC) simulations in the following sections.

IV. OBSERVABLES IN SEMICLASSICAL MONTE CARLO SIMULATIONS

To illustrate the finite-temperature properties, a collection of observables has been measured in our simulations. The following list provides the observable definitions for reference:

1. The specific heat $C_v = \frac{\beta^2}{N} [\langle E^2 \rangle - \langle E \rangle^2]$ where E is the total energy and N is the number of sites.
2. The expectation value of the operator $A(\mathbf{q}) = \frac{1}{\sqrt{N}} \langle |\mathbf{A}(\mathbf{q})| \rangle$ at the reciprocal momentum \mathbf{q} , where $\mathbf{A}(\mathbf{q}) = \sum_i \mathbf{A}_i e^{-i\mathbf{q}\cdot\mathbf{r}_i}$ is the Fourier transformation. Here, the operator \mathbf{A} can be either the dipole operator \mathbf{S} , the quadrupole operator \mathbf{Q} or any combination of SU(3) spin operators, the same as below.
3. The observable characterizing the local restriction

$$\lambda = \frac{3}{2N} \sum_{\Delta} \left(\sum_{i=1}^3 \langle \mathbf{S}_i \rangle^2 - \frac{1}{3} \left\langle \sum_{i=1}^3 \mathbf{S}_i \right\rangle^2 \right),$$

where \sum_{Δ} denotes the summation over all triangles in the Kagome lattice.

4. The susceptibility $\chi_A(\mathbf{q}) = \frac{\beta}{N} \langle |\mathbf{A}(\mathbf{q})|^2 \rangle$.

5. The susceptibility of the local restriction $\chi_\lambda = \frac{\beta}{N}[\langle \lambda^2 \rangle - \langle \lambda \rangle^2]$.
6. The fluctuation $f_A(\mathbf{q}) = \frac{1}{N}[\langle |\mathbf{A}(\mathbf{q})|^2 \rangle - \langle |\mathbf{A}(\mathbf{q})| \rangle^2]$ of the operator $\mathbf{A}(\mathbf{q})$.
7. The SSF $\mathcal{A}(\mathbf{q})$ for the operator \mathbf{A}

$$\mathcal{A}(\mathbf{q}) = \sum_{m,n} A^{mn}(\mathbf{q}),$$

where the matrix elements are given by

$$A^{mn}(\mathbf{q}) = \frac{1}{N} \langle \mathbf{A}^m(\mathbf{q}) \cdot \mathbf{A}^n(-\mathbf{q}) \rangle.$$

Here $m, n = 1, 2, 3$ are the sublattice index of a kagomé lattice. The dipolar and quadruplar SSFs can be written as $\mathcal{S}(\mathbf{q}) = \sum_{m,n} S^{mn}(\mathbf{q})$ and $\mathcal{Q}(\mathbf{q}) = \sum_{m,n} Q^{mn}(\mathbf{q})$, respectively.

8. The spin stiffness

$$\begin{aligned} \rho_{S^z}(T) &= \frac{1}{\frac{\sqrt{3}}{2}L^2} \left(\frac{\partial^2 F(\theta)}{\partial \theta^2} - \beta \left(\frac{\partial F(\theta)}{\partial \theta} \right)^2 \right) \Big|_{\theta=0} \\ &= \frac{2}{\sqrt{3}L^2} \left\{ \left\langle \frac{\partial^2 (\hat{U}_{S^z}(\theta) \mathcal{H} \hat{U}_{S^z}^\dagger(\theta))}{\partial \theta^2} \right\rangle - \beta \left\langle \left(\frac{\partial (\hat{U}_{S^z}(\theta) \mathcal{H} \hat{U}_{S^z}^\dagger(\theta))}{\partial \theta} \right)^2 \right\rangle \right\} \Big|_{\theta=0} \\ &= -\frac{2}{\sqrt{3}L^2} \left\{ \left\langle \sum_{\langle ij \rangle} \delta x_{ij}^2 \left[\frac{2J+K}{2} (S_i^x S_j^x + S_i^y S_j^y) - \frac{K}{2} (4(Q_i^{x^2-y^2} Q_j^{x^2-y^2} + Q_i^{xy} Q_j^{xy}) + Q_i^{yz} Q_j^{yz} + Q_i^{xz} Q_j^{xz}) \right] \right\rangle \right. \\ &\quad \left. - \beta \left\langle \left(\sum_{\langle ij \rangle} \delta x_{ij} \left[\frac{2J+K}{2} (S_i^x S_j^y - S_i^y S_j^x) - \frac{K}{2} (2(Q_i^{x^2-y^2} Q_j^{xy} - Q_i^{xy} Q_j^{x^2-y^2}) - (Q_i^{yz} Q_j^{xz} - Q_i^{xz} Q_j^{yz})) \right] \right)^2 \right\rangle \right\} \end{aligned}$$

where $F(\theta)$ is the free energy under a twist angle θ around the S^z axis and $\delta x_{ij} = x_i - x_j$ is the distance between the nearest neighbor spin pair i and j along the x direction. The unitary transformation $\hat{U}_{S^z}(\theta) = \exp(i\theta \sum_i x_i S_i^z)$ and $\frac{\sqrt{3}}{2}L^2$ is the Kagome lattice area.

9. The correlation function $C_A(r) = \langle \mathbf{A}(r) \cdot \mathbf{A}(0) \rangle$ where r is the distance.
10. The binder ratio $R = \langle |\mathbf{S}(\Gamma)|^4 \rangle / \langle |\mathbf{S}(\Gamma)|^2 \rangle^2$.

Here, $\langle \dots \rangle$ means the statistical average.

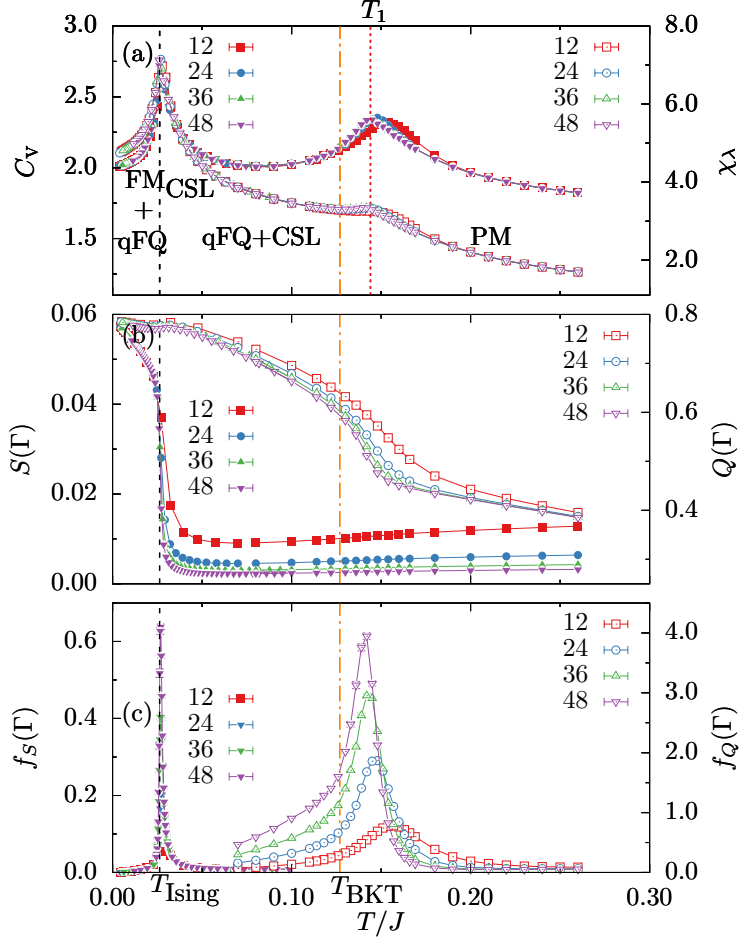


FIG. S5. The evolutions of several observables over temperature at $(K, D_z)/J = (1.0, 1.0)$. (a) Both the specific heat C_v and the susceptibility χ_λ show two peaks near temperatures T_{Ising} and T_1 . (b) The quadrupole and dipole order parameters, $Q(\Gamma)$ and $S(\Gamma)$, increase rapidly near the two specific heat peaks, respectively. (c) The fluctuations, $f_S(\Gamma)$ and $f_Q(\Gamma)$. The black dashed lines, the orange dot-dashed lines and the red dotted line indicate the Ising transition, the BKT transition and the higher-temperature specific heat peak respectively. The numerical errorbars are smaller than the point size.

V. EXTENSIVE NUMERICAL RESULTS FOR THE FINITE-TEMPERATURE PHASES AND CORRELATIONS

To determine the finite-temperature phase diagram of Fig. 1(b) shown in main text, we calculate the specific heat C_v , the susceptibility χ_λ , the dipolar order parameter $S(\Gamma)$, the quadrupolar order parameter $Q(\Gamma)$, and the fluctuations $f_S(\Gamma)$ and $f_Q(\Gamma)$ in numerical

simulations. Figure S5 shows the results for different system sizes as a function of temperature at $(K, D_z)/J = (1.0, 1.0)$. Two peaks appear in the specific heat C_v indicating large thermal fluctuations. The susceptibility χ_λ also shows a peak near the higher temperature $T_1/J = 0.144$ demonstrating the appearance of classical spin liquid. Furthermore, near T_1 , the quadrupolar order parameter $Q(\Gamma)$ starts to increase rapidly. Meanwhile, the fluctuation $f_Q(\Gamma)$ has a divergent peak near T_1 . We thus calculate the stiffness ρ_{S^z} and the susceptibility χ_{Q^t} as shown in Fig. 2 of the main text. The results indicate that there is a nematic BKT transition with an anomalous stiffness jump and it occurs at a lower temperature $T_{\text{BKT}}/J = 0.127(1)$. The inconsistency of T_1 and T_{BKT} suggests that the BKT transition is a topological phase transition and the thermal fluctuation can not reflect the transition mechanism. The same inconsistency was also reported in the two-dimensional classical XY model [5]. For comparison, we plot the higher-temperature peaks' locations in the diagram (see Fig. 1(b) in the main text). As K/J decreases, the difference between the two temperatures becomes smaller until $K/J \approx 0.546$ where they merge.

This nematic and anomalous BKT transition can be understood theoretically. In the presence of single-ion anisotropy, the symmetry of the BBQ model in Eq. (1) reduces to a lower one $U(1) \times Z_2$, but the global rotation symmetry around the S^z axis remains. According to the commutation relations Eq. (S4), it is easy to verify the following relation

$$\left[Q^{x^2-y^2}, Q^{xy} \right] = 2iS^z, \quad (\text{S49})$$

which indicates that the quadrupolar transverse operator $Q^t = (Q^{x^2-y^2}, Q^{xy})$ has the same commutation relation to the transverse spin operator $S^t = (S^x, S^y)$ up to a factor 2. This highlights that the quadrupolar transverse operators return to their initial state after rotating by only π around the S^z axis, unlike the spin dipolar transverse operators that require a full 2π rotation. As a result, the quadrupolar transverse operators still exhibit a $U(1)/Z_2 \cong U(1)$ symmetry about the S^z axis, which provides the possibility of a BKT transition. The additional factor of 2 in the commutation relation originates from the nematicity of the quadruple moments and manifests itself in the nature of topological defects. In fact, the topological defects here are Z_2 half vortices with the fractional vorticity $1/2$ instead of one in the standard XY universality class. Therefore the critical value of the stiffness at the transition T_c becomes $(\rho_{S^z})_c = 8T_c/\pi$, four times than the conventional value of $2T_c/\pi$.

As the temperature further decreases, the system enters into an $\text{FM}_{\text{CSL}} + \text{qFQ}$ phase (for

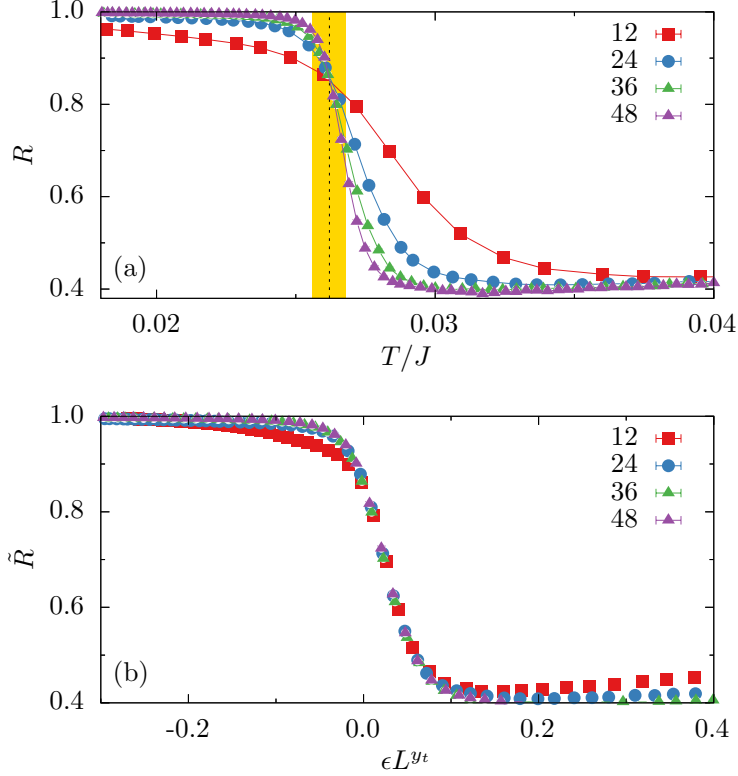


FIG. S6. The binder ratio R and the scaled binder ratio \tilde{R} over temperature for different system sizes. (a) Near the Ising transition $T_{\text{Ising}} = 0.0262$ marked by a dashed line with yellow band as errorbar, binder ratio curves for different system sizes show a crossing behavior. (b) The scale binder ratio $\tilde{R} = R - b_i L^{y_i}$ versus the scaled temperature ϵL^{y_t} with a non-universal constant $b_i = 0.40$. The exponents y_t and y_i are set to 1 and -2 , respectively, according to the $2d$ Ising universality class, and $\epsilon = (T - T_{\text{Ising}})$. For system sizes $L \geq 24$, the data collapse well onto a single curve. The numerical errorbars are smaller than the point size.

$0.546 \lesssim K/J < 2$) or an FM_{CSL} phase (for $0 < K/J \lesssim 0.546$) through a $2d$ Ising transition. To clarify this transition, the binder ratio R is calculated in numerical simulations and the results are shown in Fig. S6(a). These curves show a crossing behavior in the vicinity of the transition $T_{\text{Ising}} = 0.0262(6)$. Furthermore, Figure S6(b) shows curves of the scaled binder ratio \tilde{R} v.s. the scaled temperature $\epsilon = (T - T_{\text{Ising}})L^{y_t}$, where the critical exponents are set to $2d$ Ising universality class. The good collapse strongly advocates the transition type. Meanwhile, the susceptibility χ_λ has an obvious peak due to the fluctuation of the remaining ferromagnetic component \mathbf{S}_{FM} .

We have carried out detailed numerical simulations at $(K, D_z)/J = (0.40, 1.00)$ and

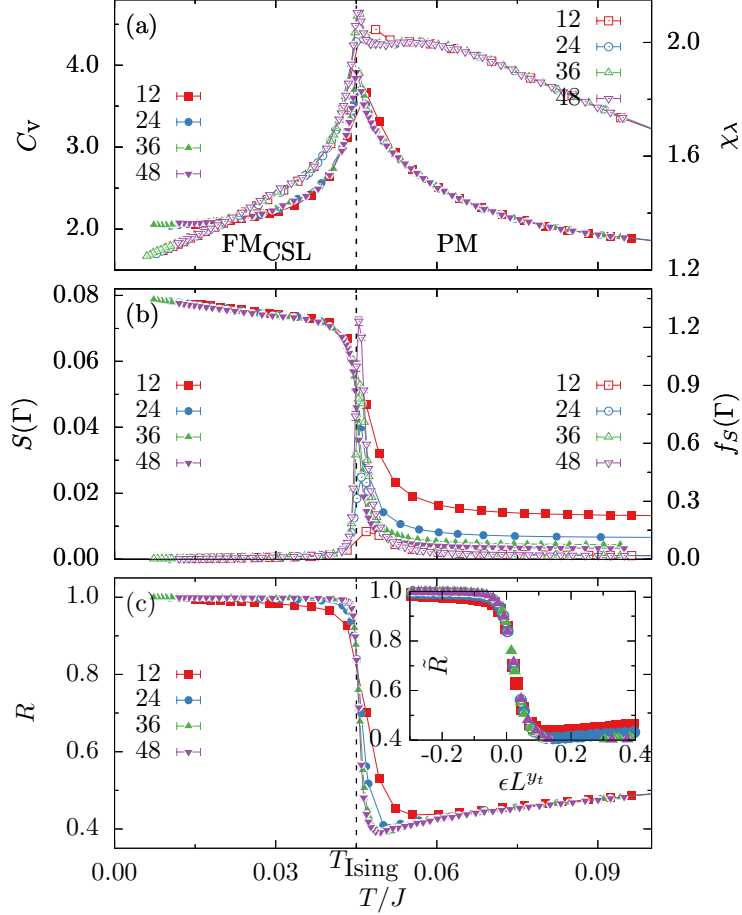


FIG. S7. The evolutions of (a) the specific heat C_v and the susceptibility χ_λ , (b) the dipole order parameter $S(\Gamma)$ and fluctuation $f_s(\Gamma)$, (c) the Binder ratio R over temperature at $(K, D_z)/J = (0.4, 1.0)$. The black dashed line indicates the Ising transition. Inset is the scale binder ratio $\tilde{R} = R - b_i L^{y_i}$ versus the scaled temperature ϵL^{y_t} with a non-universal constant. The numerical errorbars for most data points are smaller than the point size.

(2.20, 1.00) as well. The results of $(K, D_z)/J = (0.40, 1.00)$ are shown in Fig. S7 and only the Ising phase transition exists where the stiffness decreases as system size increases even in very low temperatures. The good collapse of the inset in Fig. S7(c) demonstrates that this is also a $2d$ Ising phase transition.

As mentioned in the main text, there is only a nematic BKT phase transition for $K/J > 2$. In Fig. S8, we show the results of C_v , $\tilde{\chi}_{Q^t}(\Gamma)$ and ρ_{S^z} for $(K, D_z)/J = (2.2, 1.0)$. The nematic BKT transition can still be well located at $T_{\text{BKT}} = 0.466(1)$ using the BKT RG equation marked by an orange dash-dotted line with an errorbar.

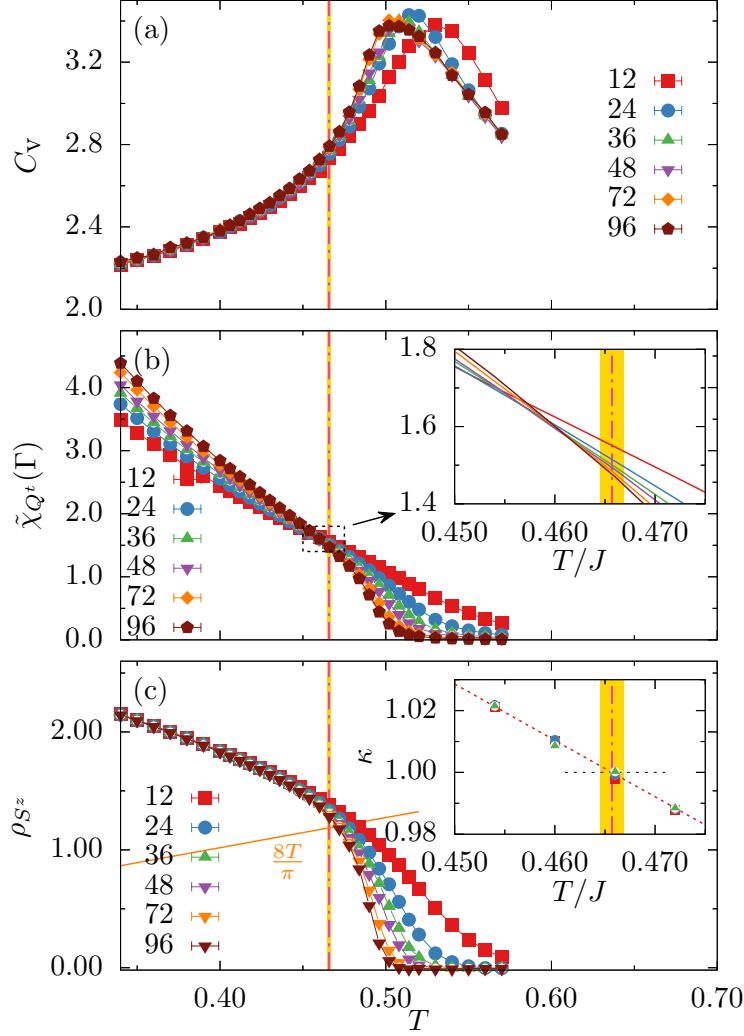


FIG. S8. The evolutions of the specific heat C_V , the susceptibility $\tilde{\chi}_{Q^t}$, and the stiffness ρ_{S^z} over temperature at $(K, D_z)/J = (2.2, 1.0)$. (a) C_V shows a round peak above the BTK transition indicating short distance correlation. (b) the scaled susceptibility $\tilde{\chi}_{Q^t}$ has an intersection near the BKT transition. (c) The stiffness ρ_{S^z} has a jump near the BTK transition. Inset in (c) shows solutions of RG equations and their linear fit of the parameter κ defined in the main text for different pairs of system sizes. The orange solid line indicates the function $f(T) = 8T/\pi$ and the BKT transition is $0.466(1)$ indicated by an orange dash-dotted line with yellow band as errorbar. The numerical errorbars are smaller than the point size.

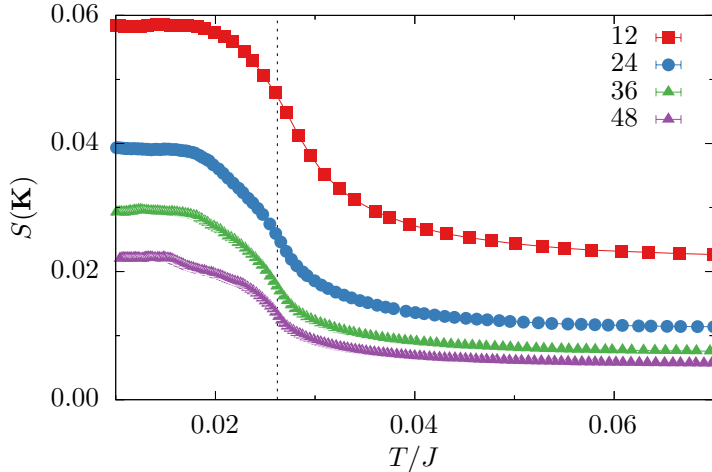


FIG. S9. The evolution of the correlation functions $\mathcal{S}(\mathbf{K})$ of the dipolar moments at $(K, D_z)/J = (1.0, 1.0)$. Within the simulated system sizes, $\mathcal{S}(\mathbf{K})$ monotonically decays even at low temperatures. The dashed line indicates the low-temperature specific heat peak. The numerical errorbars are smaller than the point size.

VI. POSSIBLE THERMAL ORDER-BY-DISORDER AT LOW TEMPERATURES

In the classical Kagome antiferromagnetic Heisenberg model, as temperature decreases, the system will go through three phases linked by two crossovers, i.e., the paramagnetic phase, the CSL phase, and the coplanar phase sequentially [6–8]. Two significant phenomena can serve as indicators that the system has entered the coplanar phase from the CSL phase: the specific heat reduces to $11/12$ from 1 and an obvious K -point peak emerges in SSF. The reduced specific heat indicates the presence of zero modes which stabilizes the coplanar order and contributes only $\frac{1}{4}T$ to the internal energy less than $\frac{1}{2}T$ contributed by a quadratic mode (one degree of freedom) [6]. When the system size is small (below a hundred), the K -point peak in SSF shows an algebraic behavior with a large correlation length even though it approaches a finite constant at the thermodynamic limit [8]. In our work, the enhancement of spin correlations at \mathbf{K} point is clearly observed as temperature decreases and its strength monotonically decays with increasing system size up to the maximum value $L = 48$ that can be simulated, as shown in Fig. S9. These results from small system sizes cannot provide sufficient evidence to support the algebraic behavior or a finite constant of $\mathcal{S}(\mathbf{K})$ at thermodynamic limit. However, Figure. S5(a) shows a different specific heat be-

havior where the value is not less than 2 (there are four DOFs for \mathbf{Z}_i). If the system has some zero modes at low temperatures, the specific heat should be smaller than 2. Based on the above results, we conclude that the system is still in a liquid state at low temperatures, but might be in conjunction with an approximate coplanar order.

VII. NUMERICAL RESULTS FOR THE SU(2) ISOTROPIC POINT ($D_z = 0$)

In the $D_z = 0$ limit, the symmetry of the model Eq. (1) is restored to SU(2). We have carried out sMC simulations in this case and obtained a finite-temperature phase diagram as shown in Fig. S10. To determine phase boundaries in the diagram, Figure. S11 illustrates the evolutions of the specific heat, two order parameters, and two fluctuations in the same fashion as the $D_z \neq 0$ case. The specific heat C_v has two peaks at a higher temperature $T_1/J = 0.117$ and a lower temperature $T_2/J = 0.056$. Near the lower one T_2 , the order parameter $S(2K)$ decreases as the system size increases, and the non-divergent behavior of the fluctuation $f_S(2K)$ indicates that the transition is a crossover. At the higher temperature T_1 , the divergence of the fluctuation $f_Q(\Gamma)$ is obvious. We further calculate the quadrupolar correlation $C_Q(r)$ at the temperature $T/J = 0.098$ which is below T_1 . It exhibits a more pronounced power-law behavior with the increase of system size, as shown in Fig. S12. These characteristics imply that the behavior near T_1 is not a second-order phase transition. In fact, there is a possible quasi-long-range FQ order below the temperature T_1 according to the situation where $D_z \neq 0$. Given the SU(2) symmetry of the model, it is worth noting that this power-law behavior may also originate from a finite-size-scaling effect due to the large correlation length which is the same as in the classical Heisenberg model in two dimensions. Therefore, we just term it an approximate-long-range FQ order (aFQ).

To further characterize the system at different temperatures, we also numerically calculate the SSFs, $\mathcal{S}(\mathbf{q})$ and $\mathcal{Q}(\mathbf{q})$ as depicted in Fig. S13. Compared with Fig. 3 in the main text, the only qualitative difference is the disappear of Γ peak in $\mathcal{S}(\mathbf{q})$ [see Fig. S13(a₃)]. Because the energy gain from the easy-axis anisotropy term $(S_i^z)^2$ is proportional to D_z , the vanishing of the FM component \mathbf{S}_{FM} is a natural result in the $D_z = 0$ limit.

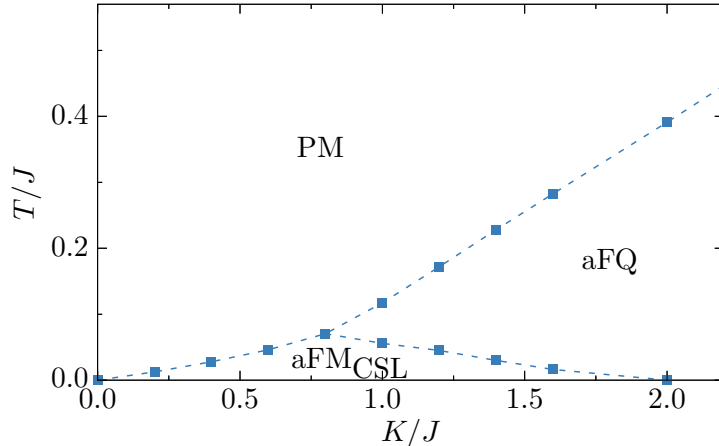


FIG. S10. The finite-temperature phase diagrams at $(K, D_z)/J = (1.0, 0.0)$. There are three regions: the PM region, the aFQ region, and the aFQ_{CSL} region. The phase boundaries are crossover and they are determined by locations of the specific heat peaks of the system size $L = 36$.

-
- [1] S. G. Johnson, The NLOpt nonlinear-optimization package, <https://github.com/stevengj/nlopt> (2007).
 - [2] A. S. Wills, R. Ballou, and C. Lacroix, Model of localized highly frustrated ferromagnetism: The kagomé spin ice, *Phys. Rev. B* **66**, 144407 (2002).
 - [3] R. Moessner and S. L. Sondhi, Theory of the [111] magnetization plateau in spin ice, *Phys. Rev. B* **68**, 064411 (2003).
 - [4] J. Carrasquilla, Z. Hao, and R. G. Melko, A two-dimensional spin liquid in quantum kagome ice, *Nature Communications* **6**, 7421 (2015).
 - [5] P. H. Nguyen and M. Boninsegni, Superfluid Transition and Specific Heat of the 2D x-y Model: Monte Carlo Simulation, *Applied Sciences* **11**, 4931 (2021).
 - [6] J. T. Chalker, P. C. W. Holdsworth, and E. F. Shender, Hidden order in a frustrated system: Properties of the Heisenberg Kagomé antiferromagnet, *Phys. Rev. Lett.* **68**, 855 (1992).
 - [7] M. E. Zhitomirsky, Octupolar ordering of classical kagome antiferromagnets in two and three dimensions, *Phys. Rev. B* **78**, 094423 (2008).
 - [8] G.-W. Chern and R. Moessner, Dipolar Order by Disorder in the Classical Heisenberg Antiferromagnet on the Kagome Lattice, *Phys. Rev. Lett.* **110**, 077201 (2013).

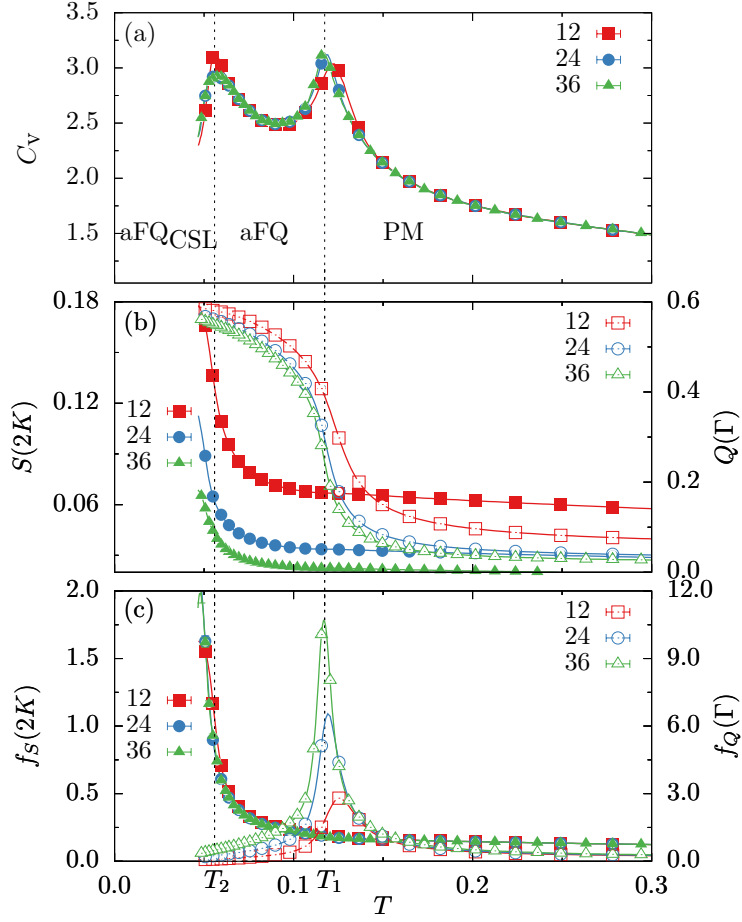


FIG. S11. The evolutions of several observables over temperature at $(K, D_z)/J = (1.0, 0.0)$. (a) The specific heat C_V . (b) The dipole and quadrupole moments, $S(2K)$ and $Q(\Gamma)$, respectively. (c) The fluctuations, $f_S(2K)$ and $f_Q(\Gamma)$. Peaks of the specific heat at temperatures T_1 and T_2 are indicated by dashed lines.

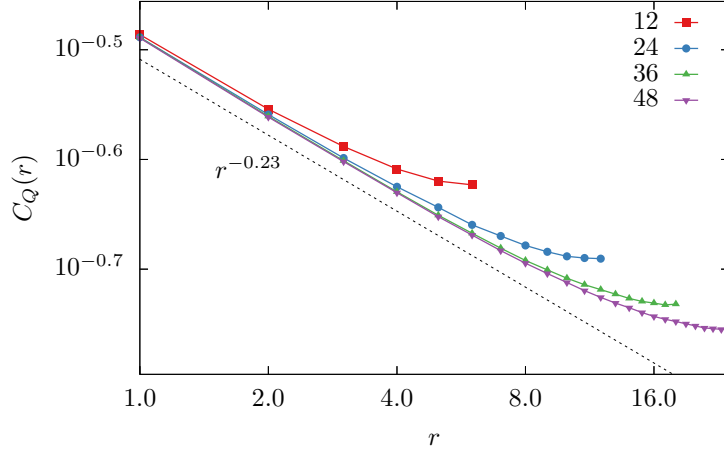


FIG. S12. The correlation functions $C_Q(r)$ of the quadrupole moments at $(K, D_z)/J = (1.0, 0.0)$ with the temperature $T/J = 0.098$. Within the simulated system sizes, the function shows a power-law behavior before the distance reaching the half linear system size. The dash line is a guide to the eye for the power-law behavior.

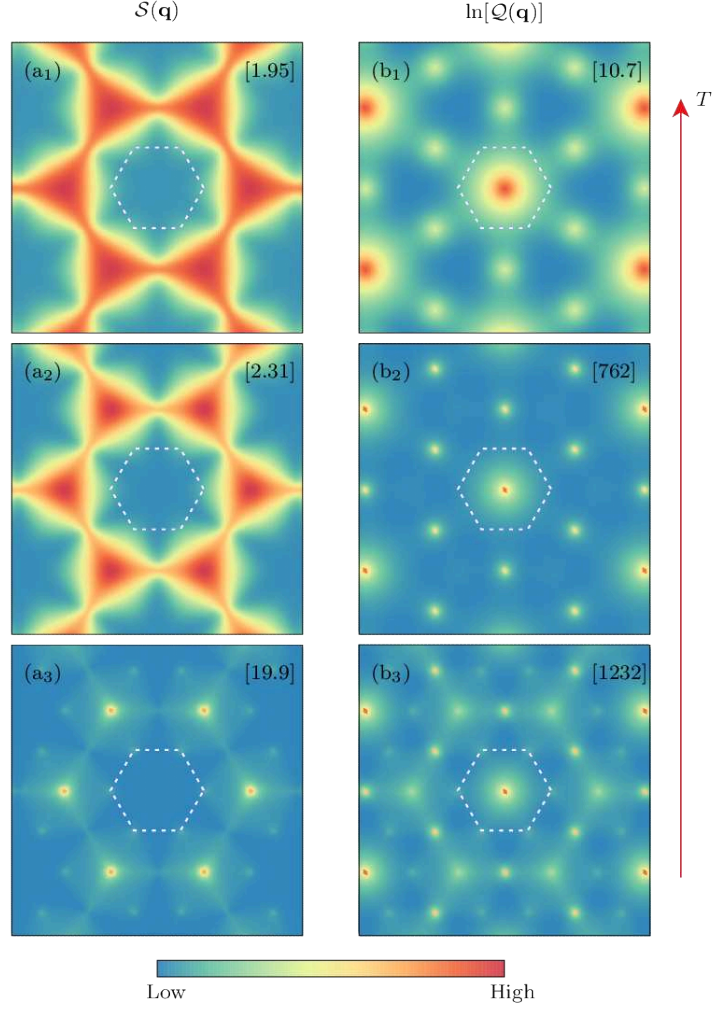


FIG. S13. The dipolar and quadrupolar SSFs, $\mathcal{S}(\mathbf{q})$ and $\mathcal{Q}(\mathbf{q})$ at different temperatures when $(K, D_z)/J = (1.0, 0.0)$ with the linear system size $L = 36$. The intensity of SSF in each graph is normalized with its maximum presented at the top right corner. From the top to bottom, the temperature decreases and the system is sequentially in the PM phase, the aFQ phase and the aFQ_{CSL} phase. The temperature for each row is equal. The dash-line hexagon indicates the first Brillouin zone. Region in the momentum space corresponds to $-4\pi \leq q_{x,y} \leq 4\pi$.